Landslides in Cascadia: Using geochronometry and spatial analysis to understand the timing, triggering and spatial distribution of slope failures in the Pacific Northwest United States

Sean R. LaHusen

A dissertation

submitted in partial fulfillment of the

requirements for the degree of

Doctor of Philosophy

University of Washington

2019

Reading Committee:

Alison R. Duvall, Chair

David R. Montgomery

Joseph Wartman

Program Authorized to Offer Degree:

Earth and Space Sciences

University of Washington

Abstract

Landslides in Cascadia: Using geochronometry and spatial analysis to understand the timing, triggering and spatial distribution of slope failures in the Pacific Northwest United States

Sean R. LaHusen

Chair of the Supervisory Committee:
Dr. Alison R. Duvall
Earth and Space Sciences

Landslides kill hundreds to thousands of people every year, cause billions of dollars in infrastructure damage, and act as important drivers of landscape evolution. In the Pacific Northwest USA, landslides routinely block roads and railways and periodically destroy homes, as recently evinced by the catastrophic 2014 Oso Landslide, which killed 43 people. Ongoing mapping efforts, aided by the ever-growing availability of bare-earth lidar elevation data, have identified tens of thousands of landslides in Washington and Oregon States. Little is known about the timing of these slope failures, and without age constraints, it is impossible to assess recurrence frequency or understand past landslide triggers. In Chapter 2, I address this problem by developing a landslide dating technique which uses surface roughness measured from lidar data as a proxy for landslide age. Unlike other landslide dating methods such as radiocarbon, exposure dating, or dendrochronology, the surface-roughness dating technique can be practically applied on a regional scale and offers an important tool for estimating landslide recurrence interval and assessing changes in landslide frequency across space. I apply this roughness dating technique to a small study area directly surrounding the 2014 Oso Landslide and show that landslides with similar destructive capacity as the Oso Landslide have been occurring within the North Fork Stillaguamish Valley every few hundred years for the last few thousand years. Importantly, this suggests that the Oso Landslide was not an anomalous event. In Chapter 3, I apply this technique on a much larger scale, estimating the ages of 9,938 manually mapped landslides across ~10,000 km^2 of similar bedrock geology in the central Oregon Coast Range, an area thought to experience violent ground shaking during Cascadia Subduction Zone earthquakes. By analyzing observed and simulated landslide frequency, I find little evidence for widespread coseismic deep-seated landsliding in this region and instead postulate that most deep-seated landslides in the inventory were triggered by rainfall. In the final research chapter, I analyze spatiotemporal patterns in deep-seated landslide frequency in the Oregon Coast Range. I find that landslide frequency decreased in the rain shadow of the Oregon Coast Range during both the early and late Holocene, times when the paleobotanical record indicates climate drying, while landslide frequency remained high on the wetter west side of the range.

TABLE OF CONTENTS

LIST OF FIGURES

LIST OF TABLES

Chapter 1. INTRODUCTION

Landslides occur whenever gravitational force overcomes the shear strength of soils and bedrock that underly Earth's surface (Lu & Godt, 2013). They act as powerful erosive agents in shaping dynamic landscapes and have profound effects on societies worldwide. Landslides are responsible for substantial loss of life and property, killing hundreds to thousands of people around the world every year (Petley, 2012). The frequency of deadly landslides suggests a fundamental lapse in our understanding of this important geomorphic process. We are limited in our ability to evaluate and mitigate the societal impacts of landslides because, while there are many models available for landslide hazard assessment, there are few sound methods for landslide risk assessment. Risk assessments require knowledge of probabilistic landslide frequency (Morgan et al., 1992; Bell and Glade, 2004; Sterlacchini et al., 2007), and extensive fieldwork is often required to obtain knowledge of the past frequency of landslide events. Typically, numerous radiocarbon or exposure dates are required to accurately constrain the timing of a single landslide, which is cost prohibitive and often impossible to apply to large inventories of landslides on the order of hundreds to tens of thousands. As a result, risk assessment remains inadequate or non-existent in many landslide-prone regions. The difficulty in determining the timing of past landslide failures also limits our understanding of the role of landslides in landscape evolution over geologic timescales. The primary contribution of this dissertation is the establishment of a new method of landslide dating that uses landslide surface roughness measured from elevation data as a quantitative proxy for landslide age. In Chapters 2, 3, and 4, I demonstrate the utility of roughness dating to estimate landslide ages on a regional scale and illuminate patterns of landslide occurrence through space and time.

In Chapter 2, I outline how the surface roughness of landslide deposits can be remotely measured and used to estimate age. This technique requires high-resolution, bare-earth elevation data, most frequently obtained from airborne laser scanning. Light detection and ranging, commonly abbreviated as ‘lidar’, allows the earth surface to be measured beneath thick vegetation, allowing for precise landslide mapping and accurate morphometric analysis (Jaboyedoff et al., 2012). By calibrating landslide deposit surface roughness measured from lidar with independent age constraints from radiocarbon dating, I show that landslide surface roughness decreases at a predictable rate with time (LaHusen et al, 2016; Booth et al., 2017). This rate can be modeled by an exponential decay function, which can then be used to estimate the age of all mapped landslides, including those without other independent age constraints, in an inventory across a regional scale. When we apply this technique to the region immediately surrounding the 2014 Oso Landslide, along the North Fork Stillaguamish River valley, we identify numerous large landslides that have occurred in the last 2,000 years that did not have previous age constraints. Importantly, this conclusion suggests a relatively high landslide recurrence frequency in this region, which equates to higher relative hazard than if these landslides were substantially older.

In Chapter 3, I use this surface roughness dating technique to investigate how deep-seated landslides in bedrock are triggered in coastal Cascadia. The vast majority of landslides around the world are triggered by earthquakes or precipitation (Keefer, 1984; Caine et al., 1980; Petley, 2012), and coastal Cascadia experiences both large earthquakes along the Cascadia Subduction Zone (CSZ) (Goldfinger et al., 2012) and characteristically wet winters (PRISM Climate Group). Full-length ruptures occur along the 1,100 km long CSZ every few hundred years (Goldfinger et al., 2012), and numerical models of these earthquakes predict violent ground shaking (Frankel et al., 2018, Wirth et al., 2018). The last large CSZ earthquake, estimated to be of magnitude 9, occurred over 300 years ago in 1700 CE. There are no written records of the landscape response to this earthquake. Moreover, while many thousands of landslides have been identified in coastal Cascadia (Burns, 2017; Burns et al., 2012; Mickelson & Slaughter., 2017), very little is known about the age of these landslides, making it difficult to determine their triggering mechanism. To explore the relative importance of CSZ earthquakes as a landslide triggers, I map 9,938 landslide deposits in the Eocene Tyee Formation and overlying Elkton Formation that comprise over 10,000 km^2 of the central Oregon Coast Range (OCR), USA. I then compile all known landslide ages from the study area, and use radiocarbon dating to establish age constraints for six additional landslides. Using these age constraints, I calibrate a surface roughness-age regression and estimate landslide ages across the study area. Through an analysis of observed and modeled landside frequency scenarios, I find little evidence that earthquakes cause widespread deep-seated landsliding in the region, despite its close proximity to the CSZ. Results from this study suggest precipitation is the primary trigger of deep-seated landsliding in the Tyee Formation of the Oregon Coast Range.

Leveraging the comprehensive landslide chronology developed in Chapter 3, I conduct a detailed analysis of spatiotemporal patterns of landsliding in Chapter 4. I first separate landslides by age into recent (<1,000 years old) and pre-Holocene subsets, and compare spatial density maps across the central OCR. Discrepancies between recent and pre-Holocene landslide density illuminate locations where landslide frequency has changed over time. I find a decrease in landslide activity along much of the eastern margin of the study area – a region that corresponds to the present-day rain shadow of the Oregon Coast Range. By examining landslide frequency through time, I find that rates of landsliding decreased during both the early and late Holocene - times when the paleobotanical record indicates climate drying (Worona & Whitlock, 1995), while landslide frequency remained high on the wetter west side. However, I do not find evidence of increased frequency on the east side during the wet middle-Holocene, which may be due to the more limited resolution of roughness dating. Still, this work suggests deep-seated landslides are sensitive to a precipitation threshold, and that during times of drying, the west side of the range remained sufficiently wet to continue regularly surpassing these rainfall triggering thresholds on a geologic timescale.

1.1 CHAPTER 1 REFERENCES

Booth, A. M., LaHusen, S. R., Duvall, A. R., & Montgomery, D. R. (2017). Holocene history of deep-seated landsliding in the North Fork Stillaguamish River valley from surface roughness analysis, radiocarbon dating, and numerical landscape evolution modeling. Journal of Geophysical Research: Earth Surface, 122(2), 456-472.

Bell, R. and Glade, T., 2004, Quantitative risk analysis for landslides – Examples from Bildudur, NW-Iceland, Natural Hazards and Earth System Sciences 4, 117-131.

Burns, B. J., Serin, D., Jones, C. B., & English, J. T. (2012) Open-File Report O-12-07, Lidar data and landslide inventory maps of the North Fork Siuslaw River and Big Elk Creek watersheds, Lane, Lincoln, and Benton Counties, Oregon

Burns, W.J. (2017). Statewide Landslide Information Database for Oregon, release 3.4: Oregon Department of Geology and Mineral Industries, Web: http://www.oregongeology.org/sub/slido/

Caine, N. (1980). The rainfall intensity-duration control of shallow landslides and debris flows. Geografiska annaler: series A, physical geography, 62(1-2), 23-27.

Frankel, A., Wirth, E., Marafi, N., Vidale, J., & Stephenson, W. (2018). Broadband synthetic seismograms for magnitude 9 earthquakes on the cascadia megathrust based on 3D simulations and stochastic synthetics, Part 1: Methodology and overall results. *Bulletin of the Seismological Society of America*, *108*(5A), 2347-2369.

Goldfinger, C., C. H. Nelson, A. E. Morey, J. E. Johnson, J. Patton, E. Karabanov, J. Gutiérrez–Pastor, A. T. Eriksson, E. Gràcia, G. Dunhill, R. J. Enkin, A. Dallimore, and T.

Vallier (2012). Turbidite event history—Methods and implications for Holocene paleoseismicity of the Cascadia subduction zone, U.S. Geological Survey Professional Paper 1661–F

Jaboyedoff, M., Oppikofer, T., Abellán, A., Derron, M. H., Loye, A., Metzger, R., & Pedrazzini, A. (2012). Use of LIDAR in landslide investigations: a review. Natural hazards, 61(1), 5-28.

Keefer, D. K. (1984). Landslides caused by earthquakes. Geological Society of America Bulletin, 95(4), 406-421.

LaHusen, S. R., Duvall, A. R., Booth, A. M., & Montgomery, D. R. (2016). Surface roughness dating of long-runout landslides near Oso, Washington (USA), reveals persistent postglacial hillslope instability. Geology, 44(2), 111-114.

Lu, N., & Godt, J. W. (2013). Hillslope hydrology and stability. Cambridge University Press.

Mickelson, K. A., & Slaughter, S. L. (2017). Washington State's new landslide inventory mapping protocol. Washington State Department of Natural Resources, Washington Geological Survey. In GSA Annual Meeting, Seattle, Washington. October (Vol. 24, No. 2017, pp. 252-5).

Morgan, G.C., Rawlings, G.E., and Sobkowicz, J.C., 1992, Evaluating total risk to communities from large debris flows. Geotechnique and natural hazards, 6-9.

Petley, D. (2012). Global patterns of loss of life from landslides. Geology, 40(10), 927-930.

PRISM Climate Group, Oregon State University, http://prism.oregonstate.edu, created 7 Oct 2019

Sterlacchini, S., Frigerio, S., Giacomelli, P., and Brambilla, M., 2007, Landslide risk analysis: a multi-disciplinary methodological approach. Natural Hazards and Earth Systems Science 7(6), 657-675.

Wirth, E. A., Frankel, A. D., Marafi, N., Vidale, J. E., & Stephenson, W. J. (2018). Broadband synthetic seismograms for magnitude 9 earthquakes on the Cascadia megathrust based on 3D simulations and stochastic synthetics, Part 2: Rupture parameters and variability. *Bulletin of the Seismological Society of America*, *108*(5A), 2370-2388.

Worona, M. A., & Whitlock, C. (1995). Late quaternary vegetation and climate history near Little Lake, central Coast Range, Oregon. Geological Society of America Bulletin, 107(7), 867-876Sterlacchini, S., Frigerio, S., Giacomelli, P., and Brambilla, M., 2007, Landslide risk analysis: a multi-disciplinary methodological approach. Natural Hazards and Earth Systems Science 7(6), 657-675.

Wirth, E. A., Frankel, A. D., Marafi, N., Vidale, J. E., & Stephenson, W. J. (2018). Broadband synthetic seismograms for magnitude 9 earthquakes on the Cascadia megathrust based on 3D simulations and stochastic synthetics, Part 2: Rupture parameters and variability. *Bulletin of the Seismological Society of America*, *108*(5A), 2370-2388.

Chapter 2. TIMING OF LONG-RUNOUT LANDSLIDES NEAR OSO, WA REVEALS PERSISTENT POSTGLACIAL HILLSLOPE INSTABILITY[1]

Establishing regional landslide chronologies is necessary to advance from hazard recognition to risk assessment and understand the evolution of landslide prone terrain. Despite recent advances in landslide mapping due to availability of high-resolution LiDAR imagery, estimating the timing of slope failures remains a challenge. Here we present a new integrated approach to dating landslides on a regional scale by augmenting quantitative surface roughness analysis with radiocarbon dating and numerical landscape modeling. We calibrate a roughness-age curve using 24 deep-seated landslides directly surrounding the catastrophic 2014 Oso Landslide along the North Fork Stillaguamish River in WA State. LiDAR bare-earth images show a high density of long-runout landslides in this region. Using our roughness-age curve, we estimate an average Holocene landslide recurrence frequency of 140 - 500 years, and show that the 2014 Oso Landslide was the latest event in an active history of slope failures throughout the Holocene. With each landslide, substantial sediment is delivered to the North Fork Stillaguamish River, driving shifts in the active channel and ultimately limiting long-term river incision. The high frequency of landslides in this area, where both uplift and incision rates are relatively low, shows that landscapes inundated by glacial sediment do not require tectonic or climatic forcing to remain highly unstable for tens of thousands of years after ice retreat.

---

[1] This chapter was published in *Geology* in 2016 with authors S.R. LaHusen, A.R. Duvall, A.M. Booth, and D. R. Montgomery

2.1 INTRODUCTION

Our ability to perform rapid and precise geomorphometric analyses of landslides has increased dramatically in the last decade with new availability of high resolution LiDAR elevation data (Roering et al., 2013). Despite much needed progress in remote landslide mapping, the challenges of dating landslides still limit our understanding of the causes of these mass movements and hamper our ability to implement full statistical assessments of landslide risk. Risk assessments require knowledge of landslide probability within a given period of time (Morgan et al., 1992; Bell and Glade, 2004; Sterlacchini et al., 2007), yet finding the appropriate dateable material across large areas can be difficult and cost prohibitive.

In this study, we use radiocarbon dates to calibrate a surface roughness-age function that predicts how landslide deposit roughness decreases over time. We apply this new approach to the area surrounding the devastating 2014 Oso Landslide, along the North Fork Stillaguamish River valley in western Washington (Figure 2.1). Much of the destruction caused by the Oso landslide was due to its impressive mobility, quantified by a low height to runout-length ratio (H:L) (Keaton et al., 2014; Iverson et al., 2015). LiDAR bare-earth imagery reveals numerous deep-seated landslides of similar morphology surrounding the Oso failure site. Cross-cutting relationships indicate that these landslides occurred over multiple generations (Haugerud, 2014), yet their absolute ages remain undetermined. Our analysis places new absolute ages on two large landslides (Rowan and Headache Creek, Figure 2.1a) and allows us to estimate the timing of failure for other landslides across the study area.

2.2 BACKGROUND

When the Cordilleran ice sheet advanced southward into the Puget Sound ~17,500 years ago, it dammed rivers flowing west from the Cascade Mountains (Porter and Swanson, 1998), filling the North Fork Stillaguamish (NFS) River valley with nearly 300m of glacial sediment. Geologic mapping indicates numerous landslide complexes have failed within this sediment (Dragovich et al., 2003), which is characterized by low permeability glaciolucustrine clays overlain by sandy advance outwash, till, and gravelly recessional outwash (Keaton et al., 2014). Similar stratigraphy is prevalent in the region and is well known to be landslide prone during and soon after high intensity or long duration precipitation (Chleborad, 2000; Coe et al., 2004). Following ice retreat around 16,400 ybp (Porter and Swanson, 1998; Beechie et al., 2001), the NFS River began incising rapidly into these mechanically weak glacial deposits, creating the modern valley relief and setting the stage for longstanding slope instability in the area. Incision rates slowed at ~12,500 ybp, when a lahar originating from Glacier Peak caused a significant area of the NFS headwaters to be captured by the adjacent Sauk River (Beechie et al., 2001) (Figure 2.1). Because large, unstable portions of relict glacial deposits still remain in the valley, such as the Whitman Bench just north of the river (Figure 2.1), the landscape is still rapidly evolving.

2.3 METHODS

In this study, we combine a surface roughness analysis with radiocarbon dates, then use results from a numerical landscape evolution model to establish a roughness-age function for the study site. We first mapped all landslide deposits on 0.9 m resolution LiDAR bare-earth imagery acquired after the Oso Landslide in 2014 by the Washington Department of Transportation. Landslide units were mapped from the presence of arcuate headscarps above hummocky terrain and verified in the field by examining exposed deposit stratigraphy and surface morphology. We also measured individual landslide headscarp dimensions, deposit area, and H:L (where H is defined as the elevation difference between the top of the headscarp and the base of the landslide deposit at the toe and L as the length from the headscarp to the distal edge of the landslide toe) using ESRI ArcMap 10 software (Supplementary Table 2.1). Measurement of H:L for each landslide quantifies its mobility and allows us to compare the style of past slope failures in the valley with that of the 2014 Oso Landslide.

We use radiocarbon dates of woody debris to obtain absolute ages for the Rowan and Headache Creek landslides, and also date a terrace 4 m above the active river channel (Figure 2.1). The age of the Rowan Landslide was determined using carbon dates from six samples of woody debris entrained at different sites within the landslide deposit; four from the toe and two from the main body of the slide (Samples 1-6 in Figure 2.1). Samples from the toe were excavated from exposed landslide deposit within cutbanks along the NFS River, whereas samples from the main body were found protruding from the wall of a 5m deep stream gully incised into the landslide deposit. Wood samples are interpreted to be from trees killed during the landslide event, and therefore represent maximum landslide age. Three radiocarbon dates from bark collected off of buried logs exposed in the eastern margin of the 2014 Oso Landslide (Keaton et al., 2014) constrain the timing of the Headache Creek Landslide (Samples 8-10 in Figure 2.1). All samples were analyzed at AMS Direct in Bothell, WA, and then calibrated using OxCal 4.2 software (Ramsey, 2009).

For landslides without absolute age constraints, we use these radiocarbon dates to calibrate a surface roughness analysis, thereby extending age estimation to the undated landslides. Previous studies have used surface roughness as a proxy for relative age of landforms such as alluvial fans and landslides (Bull, 1977; Matmon et al., 2006; Glenn et al., 2006; Frankel and Dolan, 2007). In a study of roughness elements within desert fans, Matmon et al. (2006) demonstrated that these surfaces smooth non-linearly with age. Surface roughness has also been used for automated mapping of landslide features (Booth et al., 2009). Here we calculate surface roughness for each landslide deposit using the average standard deviation of slope (SDS) within a 15m x 15m roving window (this window size best captures the wavelength of the of landslide hummocks). This method is simple to calculate and does not require de-trending to account for overall landform slope (Berti et al., 2013) (Supplementary Figure 2.1).

In order to apply measures of SDS as a landslide age proxy, we assume that rough terrain features throughout the study area smooth over time at approximately the same rate due to the similar climate and lithology (Keaton et al., 2014). The processes responsible for smoothing landslides in our study area are assumed to be primarily creeping, gravity-driven processes causing downslope diffusion of landslide material. We also assume similar initial roughness for fresh landslide deposits, which is supported by the morphological similarity between landslides in the study area. To remove the effect of increased roughness from gullying, all gullies incised more than 2m into landslide deposits were removed from the roughness analysis manually (Supplementary Figure 2.1). Other roughness biases, such as headscarps, roads, and modern NFS River erosional contacts, were also removed prior to the analysis so that only the natural landslide deposit surfaces were measured.

The average SDS values for landslides of known age are then plotted against four absolute age constraints on landsliding: the recent Oso Landslide, the Rowan Landslide, the Headache Creek Landslide, and a maximum limit on landslide deposits that overly the modern NFS floodplain. This maximum limit is set by the radiocarbon age of the terrace remnant that sits 4 m above the modern floodplain, and we assign this age to the landslide deposit with the lowest SDS value. Assuming that the landscape smoothing over time is due to linear soil diffusion, we also employ a numerical landscape evolution model to determine the regression that best represents the data. The numerical model simulated the change in the land surface elevation, z, with time, t, as $\partial z/\partial t = D\nabla^2 z$, where D is a constant (Press, 2007), using the Oso landslide deposit from the 2014 digital elevation data as the initial condition (Figure 2.5).

2.4 RESULTS

Landslide Mapping

We remotely mapped 24 individual landslide deposits within a six kilometer long section of the NFS River valley using the 0.9 m resolution LiDAR imagery, similar to what was mapped by Haugerud (2014). H:L analysis reveals several past landslides with considerable mobility, with 30% having H:L values of 0.20 or less (Supplementary Table 2.1). The largest landslide deposit in the valley, the Rowan Landslide, covers nearly double the area of the 2014 Oso Landslide (Figure 2.1a) and exhibits an H:L ratio of 0.10, comparable to recent estimations of the Oso Landslide (Iverson et al., 2015). The longitudinal morphology of the Rowan deposit also closely resembles the Oso Landslide, with a steep main headscarp, similar extensional faulted blocks in the main body of the deposit, and a hummocky distal section that likely represents a more fluidized portion of the landslide (Figure 2.1b).

^{14}C Dating

Calibrated radiocarbon dates from six samples of wood entrained in the Rowan Landslide deposit (Figure 2.1a) indicate that failure occurred between 319-694 ybp, with an average calibrated age of 518 ybp (Supplementary Table 2.2). Radiocarbon dates from the three samples at Headache Creek Landslide, which lies adjacent to the Oso Landslide (Figure 2.1a), place the time of failure between 5757-6278 ybp[1] (Supplementary Table 2.2). An intact tree trunk from within the fluvial terrace overrun by the Rowan Landslide (Sample 7 in Figure 2.1a) dates to 11,406-11,978 calibrated ybp.

Calibrated Surface Roughness Dating

The standard deviation of slope of the 24 mapped landslides ranges from 4.044 to 8.018 within the study area (Supplementary Table 2.1). When plotted against absolute age of the dated landslide deposits, these data show landslide surface roughness decays with time at a decreasing rate (Figure 2.2), similar to the trend observed in desert alluvial fans (Hetz et al., 2013).

Results from the numerical landscape evolution model, which calculates SDS of the Oso landslide deposit at each time-step for 12,000 years, suggests the smoothing of landslide deposits over time is well-fit by an exponential decay function (see supplementary materials for model description) (Figure 2.2a). Using Sigma Plot software, we then fit a single exponential function to the four observed roughness-age data points, which yields the following function: $T = 3519500*^{e-1.3976*R}$, where T = estimated age (ybp) and R = average SDS of landslide deposit (Figure 2.2b). Using this function, we estimate the age of each landslide in the study area, and bin landslides into the following four age classes: A (early Holocene): > 5,000 ybp, B (mid Holocene): 2,000-5,000 ybp, C (late Holocene): 500-2,000 ybp, and D (recent): < 500 ybp (Figure 2.3).

2.5 DISCUSSION & CONCLUSIONS

Results from this study show that the North Fork Stillaguamish River valley is a highly unstable postglacial landscape where the process of glacial sediment evacuation is ongoing, facilitated primarily though long runout landslides. Although the Oso and Rowan landslides have the lowest measured H:L ratios, many landslides in the valley with higher H:L ratios have been substantially eroded by the NFS River, such that the present-day length of deposits is not representative of the true runout length. Many of these landslides share similar headscarp and deposit morphology to Oso and Rowan, which indicates that these landslides may have been similarly mobile. Other, less eroded, landslides with higher H:L values are topographically constricted by opposing valley walls, which act as barriers that limit runout length (Corominas, 1996).

An average landslide frequency calculated using the total number of landslides in the study area and assuming no landslides are older than 12,000 ybp yields a value of one event per 500 years. However, the high number of young landslides here suggests a preservation bias caused by older landslide deposits being eroded or overrun by younger slope failures. When only the last 2,000 years are considered, the average landslide frequency is substantially higher: one event per 140 years.

Our results reveal that long-runout landslides have occurred along the North Fork Stillaguamish River throughout the late Holocene. We suspect that mass-wasting events in the area are related to long-term spatial patterns in NFS river erosion, and that landslides, in turn, impart a strong control on river location. The NFS River floodplain was likely covered completely when the Rowan Landslide failed, and pinned the river against the south side of the valley (Figure 2.1). A fluvial erosional contact evident in LiDAR images at the toe of an older landslide adjacent to the Rowan Landslide suggests that the NFS River was located on the north side of the valley prior to the Rowan Landslide (Figure 2.3b). If so, the NFS River would have been displaced some 600m to the south when the Rowan Landslide failed. When landslides such as this cross the entire valley floor, they may shift the location of the active river channel by hundreds of meters towards the opposing valley wall, leading to increased fluvial erosion where the channel is confined. We suspect that landslides from one side of the valley repeatedly set up slope failures to occur on the opposite side, over time creating an alternating pattern of landsliding (Safran et al., 2011).

In addition to shifting plan view river patterns, the Holocene history of long-runout landslides in the Stillaguamish Valley may also have affected the river's incision history. Dated river terraces show that after incision through 300m of glacial sediment within the first 4,000 years after ice retreat, the river generated only a few meters of relief in the subsequent 12,000 years. This dramatic reduction of incision rates likely reflects a decrease in stream power due to headwater diversion following a 12,500 ybp lahar from Glacier Peak (Beechie, et al., 2001) and a large influx of sediment from repeated landslides suppressing incision (Sklar and Dietrich, 2004; 2006; Finnegan et al., 2007) or triggering aggradation (Korup, 2006; Ouimet et al., 2007). Deflections of the river to opposing valley walls also widen the valley, setting the stage for future destabilization of hillslopes by undercutting valley walls.

The evidence for postglacial instability throughout the Holocene indicates that the mechanically weak glacial stratigraphy found in this valley, which is typical of ice-sheet advances around the world, presents an ongoing landslide hazard that will continue until the removal of this material from the valley. Hence, even in the absence of rapid uplift or incision, the process of evacuating potentially unstable glacial sediment may result in persistent instability for tens of thousands of years after ice retreat. Our analysis, however, shows that remote sensing data can be used to quantitatively estimate landslide age, and thereby assess landslide risk, when surface roughness is calibrated with even a limited set of absolute dates.

2.6 ACKNOWLEDGEMENTS

We acknowledge the National Science Foundation (grant EAR – 1331412), the Geological Society of America (graduate student grant to S.L.), and the University of Washington Quaternary Research Center for support of this research. We thank the Washington Department of Natural Resources for site access and Stephen Slaughter and Camille Collett for assistance in the field. This manuscript benefited from discussions with Amit Mushkin.

2.7 FIGURES

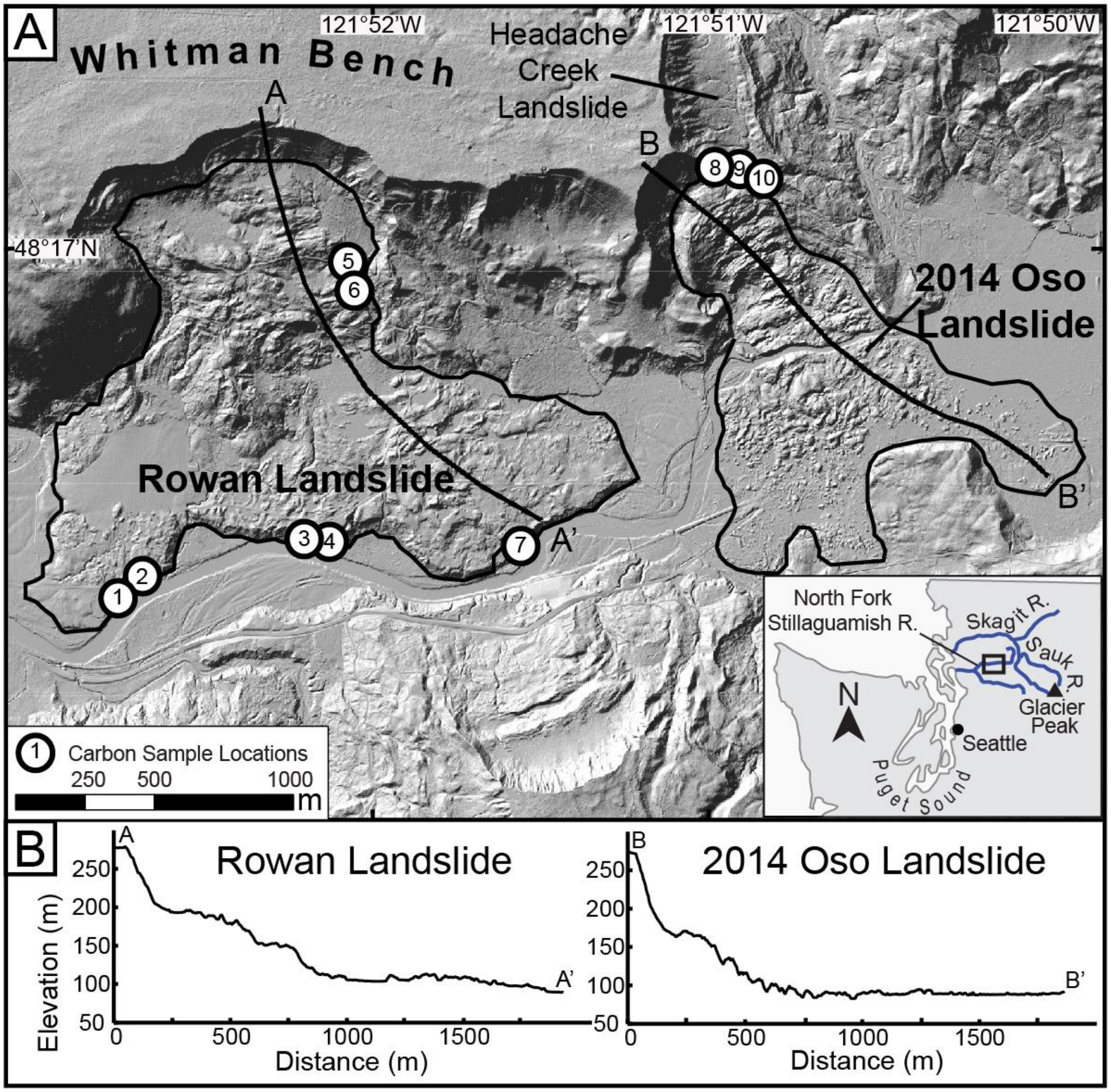

Figure 2.1. **A.** LiDAR bare-earth imagery showing the Rowan Landslide and the 2014 Oso Landslides in the North Fork Stillaguamish River Valley, with ^{14}C samples shown as numbered circles and the study area shown as a black box in the inset map. **B.** Elevation profiles of the Rowan and 2014 Oso landslides, from scarp to deposit toe.

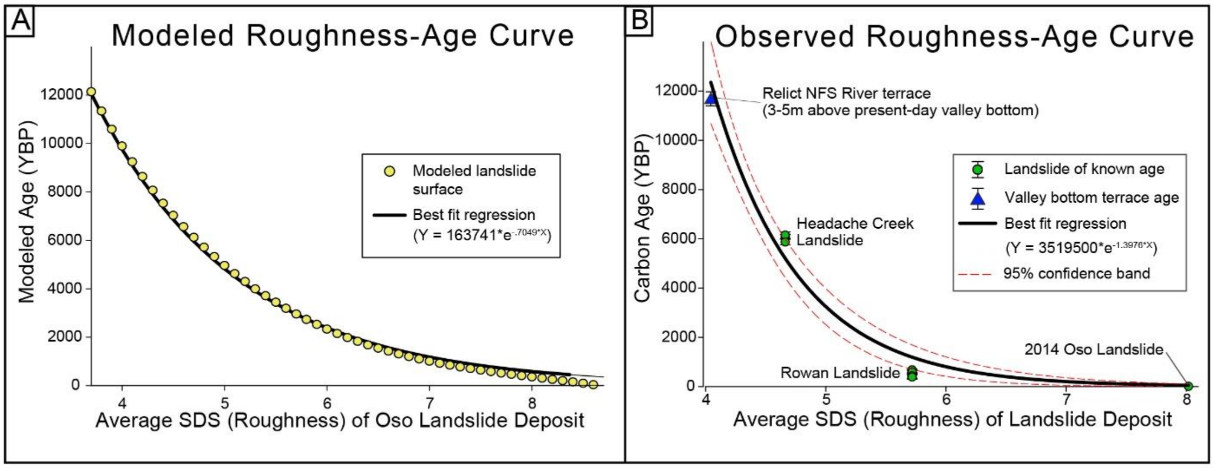

Figure 2.2. **A.** Single exponential decay function fit to the linear diffusion model results, where the 2014 Oso Landslide elevation data is used as the initial condition at time *t* = 0. **B.** Calibrated surface roughness-age curve used to estimate landslide frequency across the study area. ^{14}C dates plotted against standard deviation of slope (roughness), with a maximum limit on landslide age in the study area constrained by the age of valley bottom terrace. A single exponential function is fit to these data, and used to predict the age of landslides for which no absolute age information is available.

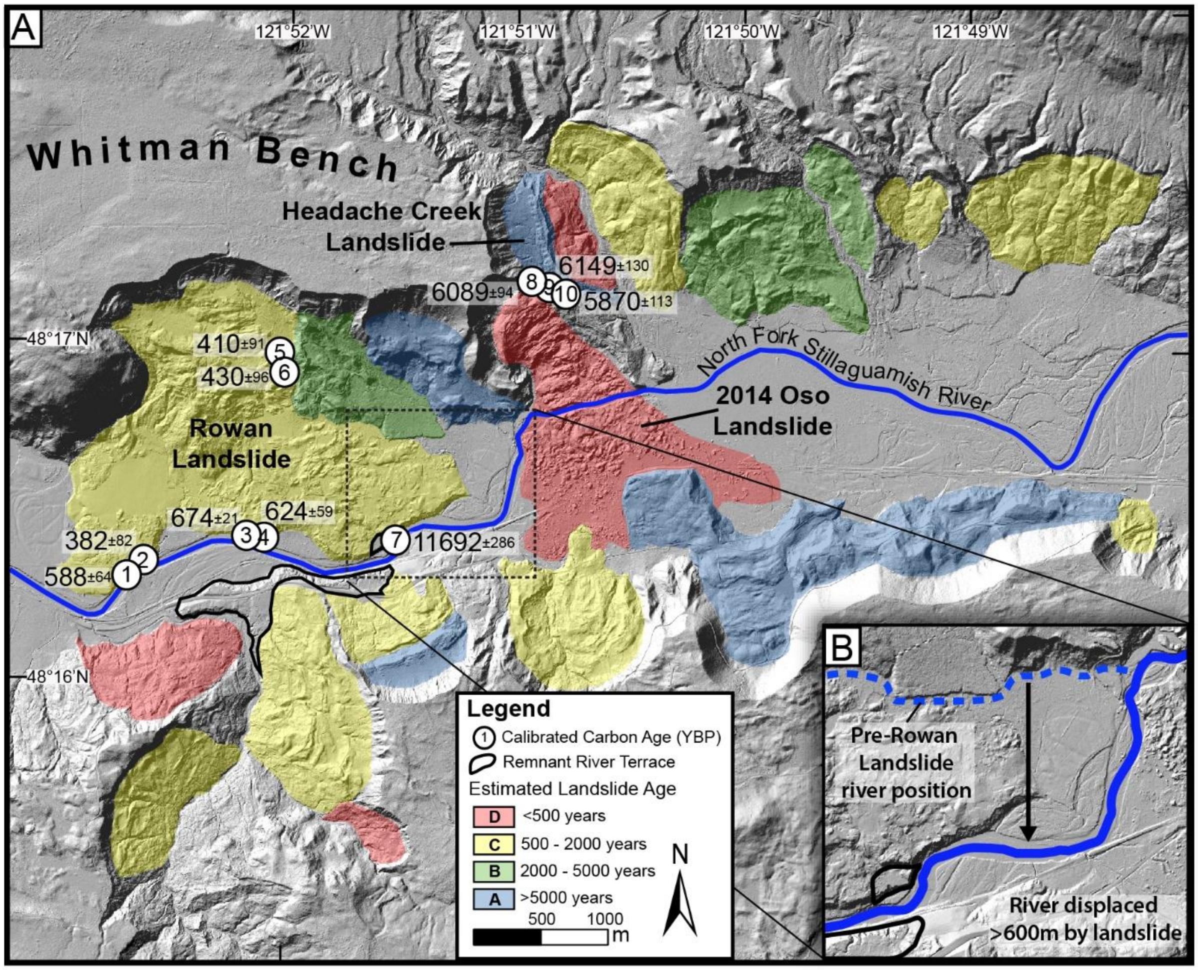

Figure 2.3. **A.** LiDAR bare-earth imagery of the study area, showing all mapped landslides colored by estimated age. Landslides across the study area are binned into 4 age classes (7 class 3 class B, 10 class C, and 4 class D) based on estimated age from the surface roughness-age regression. Predicted age classes agree well with cross-cutting relationships between landslides. **B.** Blow-up map showing inferred river position (dashed line) prior to the Rowan Landslide ~500ybp, based on erosional contact on an older landslide deposit. The current river position (solid line) suggests the active channel was displaced at least 600m when the Rowan Landslide occurred.

2.8 CHAPTER 2 REFERENCES

Berti, M., Corsini, A., & Daehne, A., 2013, Comparative analysis of surface roughness algorithms for the identification of active landslides. *Geomorphology* **182,** 1-18.

Booth, A. M., Roering, J. J., & Perron, J. T., 2009, Automated landslide mapping using spectral analysis and high-resolution topographic data: Puget Sound lowlands, Washington, and Portland Hills, Oregon. *Geomorphology* **109,** 132-147.

Beechie, T. J., Collins, B. D., & Pess, G. R., 2001, Holocene and recent geomorphic processes, land use, and salmonid habitat in two north Puget Sound river basins. *Geomorphic Processes and Riverine Habitat*, Water Science and Application **4,** 37-54.

Bell, R. and Glade, T., 2004, Quantitative risk analysis for landslides – Examples from Bildudur, NW-Iceland, Natural Hazards and Earth System Sciences **4**, 117-131.

Bull, W. B., 1977, The alluvial-fan environment. *Progress in Physical Geography* **1,** 222-270.

Chleborad, A. F., 2000, Preliminary method for anticipating the occurrence of precipitation-induced landslides in Seattle, Washington. USGS Open-File Report **2000-469**.

Coe, J. A., Michael, J. A., Crovelli, R. A., Savage, W. Z., Laprade, W. T., & Nashem, W. D., 2004, Probabilistic assessment of precipitation-triggered landslides using historical records of landslide occurrence, Seattle, Washington. *Environmental & Engineering Geoscience* **10,** 103-122.

Corominas, J., 1996, The angle of reach as a mobility index for small and large landslides. *Canadian Geotechnical Journal* **33,** 260-271.

Dragovich, J., Stanton, B., Lingley, W., Griesel, G., & Polenz, M., 2003, Geologic Map of the Mount Higgins 7.5-minute Quadrangle, Skagit and Snohomish Counties, Washington. Washington Division of Geology and Earth Resources Open File Report **2003-12**.

Finnegan, N. J., Sklar, L. S., & Fuller, T. K., 2007, Interplay of sediment supply, river incision, and channel morphology revealed by the transient evolution of an experimental bedrock channel. *Journal of Geophysical Research: Earth Surface* **112,** F03S11.

Frankel, K. L. & Dolan, J. F., 2007, Characterizing arid region alluvial fan surface roughness with airborne laser swath mapping digital topographic data. *Journal of Geophysical Research: Earth Surface*, **112,** F02025.

Glenn, N. F., Streutker, D. R., Chadwick, D. J., Thackray, G. D., & Dorsch, S. J., 2006, Analysis of LiDAR-derived topographic information for characterizing and differentiating landslide morphology and activity. *Geomorphology* **73,** 131-148.

Haugerud, R.A., 2014, Preliminary interpretation of pre-2014 landslide deposits in the vicinity of Oso, Washington: U.S. Geological Survey Open-File Report **2014–1065**.

Hetz, G., Mushkin, A., Blumberg, D. G., & Baer, G., 2013, Estimating the surface age of arid-zone alluvial fans using spaceborne radar data. *SPIE Remote Sensing* **8891.**

Iverson, R. M., et al., 2015, Landslide mobility and hazards: implications of the 2014 Oso disaster. *Earth and Planetary Science Letters* **412,** 197-208.

Keaton, J. R., et al., 2014, The 22 March 2014 Oso Landslide, Snohomish County, Washington. Geotechnical Extreme Events Reconnaissance Association Report **GEER-036**.

Korup, O., 2006, Rock-slope failure and the river long profile. *Geology* **34,** 45-48.

Larsen, I. J., & Montgomery, D. R., 2012, Landslide erosion coupled to tectonics and river incision. *Nature Geoscience*, **5**, 468-473.

Matmon, A., Nichols, K., & Finkel, R., 2006, Isotopic insights into smoothening of abandoned fan surfaces, southern California. *Quaternary Research* **66,** 109-118.

Morgan, G.C., Rawlings, G.E., and Sobkowicz, J.C., 1992, Evaluating total risk to communities from large debris flows. *Geotechnique and natural hazards*, 6-9.

Ouimet, W. B., Whipple, K. X., Royden, L. H., Sun, Z., & Chen, Z., 2007, The influence of large landslides on river incision in a transient landscape: Eastern margin of the Tibetan Plateau (Sichuan, China). *Geological Society of America Bulletin* **119,** 1462-1476.

Porter, S. C. & Swanson, T. W., 1998, Radiocarbon age constraints on rates of advance and retreat of the Puget lobe of the Cordilleran ice sheet during the last glaciation. *Quaternary Research* **50**, 205-213.

Press, W. H., 2007, *Numerical recipes 3rd edition: The Art of Scientific Computing*. Cambridge University Press.

Ramsey, C. B., 2009, Bayesian analysis of radiocarbon dates. *Radiocarbon* **51,** 337-360.

Roering, J.J., Mackey, B.H., Marshall, J.A., Sweeney, K.E., Deligne, N.I., Booth, A.M., Handwerger, A.L., and Cerovski-Darriau, C., 2013, 'You are HERE': Connecting the dots with airborne lidar for geomorphic fieldwork. Geomorphology **200**, doi:10.1016/j.geomorph.2013.04.009.

Safran, E. B., Anderson, S. W., Mills-Novoa, M., House, P. K., & Ely, L., 2011, Controls on large landslide distribution and implications for the geomorphic evolution of the southern interior Columbia River basin. *Geological Society of America Bulletin* **123,** 1851-1862.

Sklar, L. S. & Dietrich, W. E., 2004, A mechanistic model for river incision into bedrock by saltating bed load. *Water Resources Research* **40,** W06301.

Sklar, L. S. & Dietrich, W. E., 2006, The role of sediment in controlling steady-state bedrock channel slope: Implications of the saltation–abrasion incision model. *Geomorphology* **82,** 58-83.

Sterlacchini, S., Frigerio, S., Giacomelli, P., and Brambilla, M., 2007, Landslide risk analysis: a multi-disciplinary methodological approach. *Natural Hazards and Earth Systems Science* **7(6)**, 657-675.

2.9 APPENDIX TO CHAPTER 2

Supplementary Text

This study applies a new regional approach to dating landslide deposits that combines large-scale geomorphic analysis of LiDAR imagery with absolute age dating of selected landslides in order to predict ages of all landslides across the study area. We mapped all landslides within a ~6km long section of the North Fork Stillaguamish River valley, directly surrounding the catastrophic 2014 Oso Landslide (SM Figure 2.1). Landslides were mapped from 0.9m resolution LiDAR bare-earth imagery acquired by the Washington State Department of Transportation (2014). The criteria we used to map landslide units were the presence of an arcuate headscarp overlying a hummocky portion of terrain with evidence of displacement in a down-gradient direction. This LiDAR data was also used for additional geomorphometric analyses of each landslide deposit, including standard deviation of slope (a measure of surface roughness), total height, and total length (SM Table 2.1). We then verified digitally mapped landslides in the field by examining exposed deposit stratigraphy and surface morphology.

To measure surface roughness for each mapped landslide unit, we calculated average standard deviation of slope (SDS) from the LiDAR data using a 15m x 15m roving window in ArcMap 10. In order to apply measures of SDS as a landslide age proxy, we assumed that rough terrain features throughout the study area smoothed over time at approximately the same rate due to the similar climate and lithology (Keaton, et al., 2014). We also assumed similar initial roughness for fresh landslide deposits, which is supported by the morphological similarity between landslides in the study area. To remove the effect of increased roughness from gullying, all gullies incised more than 2m into landslide deposits were removed manually from the digitally mapped landslide polygons so they would not affect the roughness analysis (SM Figure 2.1). Other roughness biases, such as headscarps, roads, and modern NFS River erosional contacts, were also removed prior to the analysis so that only the natural landslide deposit surfaces were measured. SDS was calculated for each cell in the study area, then, an average value of SDS was determined for each of the 24 mapped landslide polygons (SM Figure 2.1). This average SDS value is used to estimate landslide age using our calibrated roughness-age curve.

Radiocarbon ages of woody debris provided absolute ages for the Rowan and Headache Creek landslides (SM Table 2.2). Wood samples are interpreted to be from trees killed during the landslide event, and therefore represent maximum landslide age. The age of the Rowan Landslide was determined using new carbon dates from six samples of woody debris entrained at different sites within the landslide deposit; four from the toe and two from the main body of the slide (Samples 1-6 in Figure 2.1; SM Table 2.2). These ages place bounds on the timing of failure of this landslide between 300-694 calibrated ybp (from lower end 1σ error range of youngest sample age to upper 1σ error range of oldest sample age). Samples from the toe were excavated from exposed landslide deposit within cutbanks along the NFS River, whereas samples from the main body were found protruding from the wall of a 5m deep stream gully incised into the landslide deposit. Three radiocarbon dates from bark collected off of buried logs exposed in the eastern margin of the 2014 Oso Landslide (Keaton, et al., 2014) constrain the timing of the Headache Creek Landslide to 5757-6278 ca. ybp (Samples 8-10 in Figure 2.1; SM Table 2.2). All wood samples were analyzed at AMS Direct in Bothell, WA, and then calibrated using OxCal 4.2 software (Ramsey, 2009).

We plot radiometric carbon dates of landslide deposits against a quantitative analysis of surface roughness (Figure 2.2). To determine what type of regression to use to calibrate the age-roughness curve, we applied a linear diffusive landscape evolution model to the Oso landslide deposit which has an initial age of zero. The numerical model simulated the change in the land surface elevation, z, with time, t, as $\partial z/\partial t = D\nabla^2 z$, where D is a constant. Using the Oso landslide deposit as the initial condition, we integrated this equation forward in time using an alternating-direction implicit method (Press, 2007), and measured SDS of the landslide deposit at each time step. A value of $D = 0.001$ m^2/yr resulted in the minimum RMS misfit between the modeled surface roughness and observed surface roughness for the four data points in the age-roughness calibration curve (Figure 2.2), and both the observed and modeled age vs. roughness curves are well-fit by exponential functions. We then fit a single exponential regression to the observed age-roughness plot (Figure 2.2b) and use this function to estimate the age of the other mapped landslides across the study area for which absolute age information does not exist. Observed SDS ranges from 4.044m to 8.018m within the study area, which corresponds to estimated ages from 50 ybp to 12,000 using the best-fit function (SM Table 2.1).

Supplementary Figures and Tables

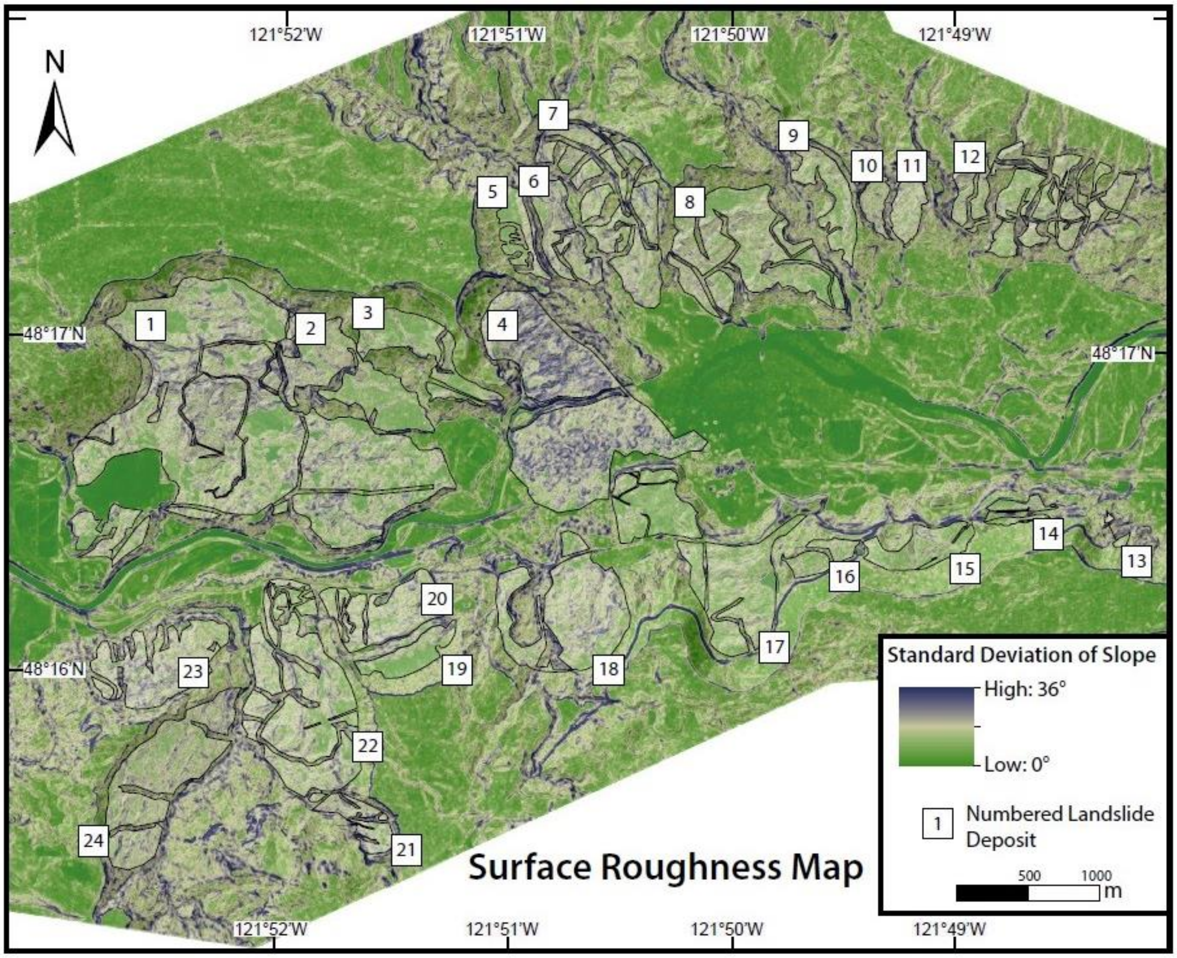

Figure 2.4. Map showing surface roughness of mapped landslide polygons across the study area. Land surface is colored by standard deviation of slope (SDS), ranging from low SDS shown in green (0°) to high SDS shown in blue (up to 36°). Opaque landslide polygons used in roughness analysis are numbered, and correspond with numbers in SM Table 2.1. These polygons reflect the removal of roads, gullies, and fluvial erosive contacts from the landslide polygons displayed in Figure 2.3.

Table 2.1. Morphological attributes and estimated age for each landslide.

ID #	**Name**	**Area (km^2)**	**Headscarp height (m)**	**Height (m)**	**Length (m)**	**H:L Ratio**	**SDS (m)**	**Estimated age**
1	Rowan Landslide	1.99	90	200	1980	0.10	5.72	1200
2		0.33	100	180	910	0.20	5.11	2800
3		0.28	90	190	790	0.24	4.40	7500
4	2014 Oso Landslide	0.94	110	190	2010	0.09	8.02	50
5	Headache Creek Landslide	0.27	70	140	580	0.24	4.57	5900
6		0.13	20	60	220	0.27	7.16	160
7		0.42	20	130	410	0.32	6.30	530
8		0.57	50	160	910	0.18	5.13	2700
9		0.14	30	90	300	0.30	5.09	2800
10		0.04	10	70	200	0.35	6.10	700
11		0.07	30	90	340	0.26	5.81	1000
12		0.47	20	160	620	0.26	5.53	1600
13		0.06	90	150	440	0.34	5.55	1500
14		0.15	110	160	460	0.35	4.38	7700
15		0.26	100	160	580	0.28	4.46	7000
16		0.14	110	150	460	0.33	4.60	5700
17		0.56	80	180	1400	0.13	4.19	10000
18		0.47	90	130	1010	0.13	6.13	670
19		0.12	60	160	730	0.22	4.04	12000
20		0.21	30	100	460	0.22	6.26	560
21		0.07	30	70	240	0.29	6.96	210
22		0.58	50	150	790	0.19	5.72	1200
23		0.32	40	160	550	0.29	6.57	360
24		0.31	40	120	490	0.24	6.08	710

Table 2.2. Radiocarbon dating results

Sample #	**Sample Material**	**Deposit Type**	**Radiocarbon Age (1σ error)**	**Calibrated YBP (1σ error range)**	**Location (Long;Lat)**
1	Wood (broken branch)	Rowan landslide	572±37	524-651	-121.879; 48.272
2	Wood (trunk fragment)	Rowan landslide	307±30	300-464	-121.877; 48.272
3	Wood (trunk fragment)	Rowan landslide	722±24	653-694	-121.869; 48.274
4	Wood (trunk fragment)	Rowan landslide	693±24	565-683	-121.869; 48.274
5	Bark (intact trunk)	Rowan landslide	368±23	319-500	-121.876; 48.283
6	Wood (outer trunk)	Rowan landslide	426±29	334-526	-121.876; 48.283
7	Wood (outer trunk)	Fluvial terrace buried by Rowan landslide	10,103±37	11,406-11,978	-121.858; 48.274
8	Bark (intact tree trunk)	Headache Creek landslide	5304 ±28	5995-6182	-121.850; 48.287
9	Bark (intact tree trunk)	Headache Creek landslide	5371 ±28	6019-6278	-121.849; 48.286
10	Bark (intact tree trunk)	Headache Creek landslide	5138 ±27	5757-5983	-121.848; 48.286

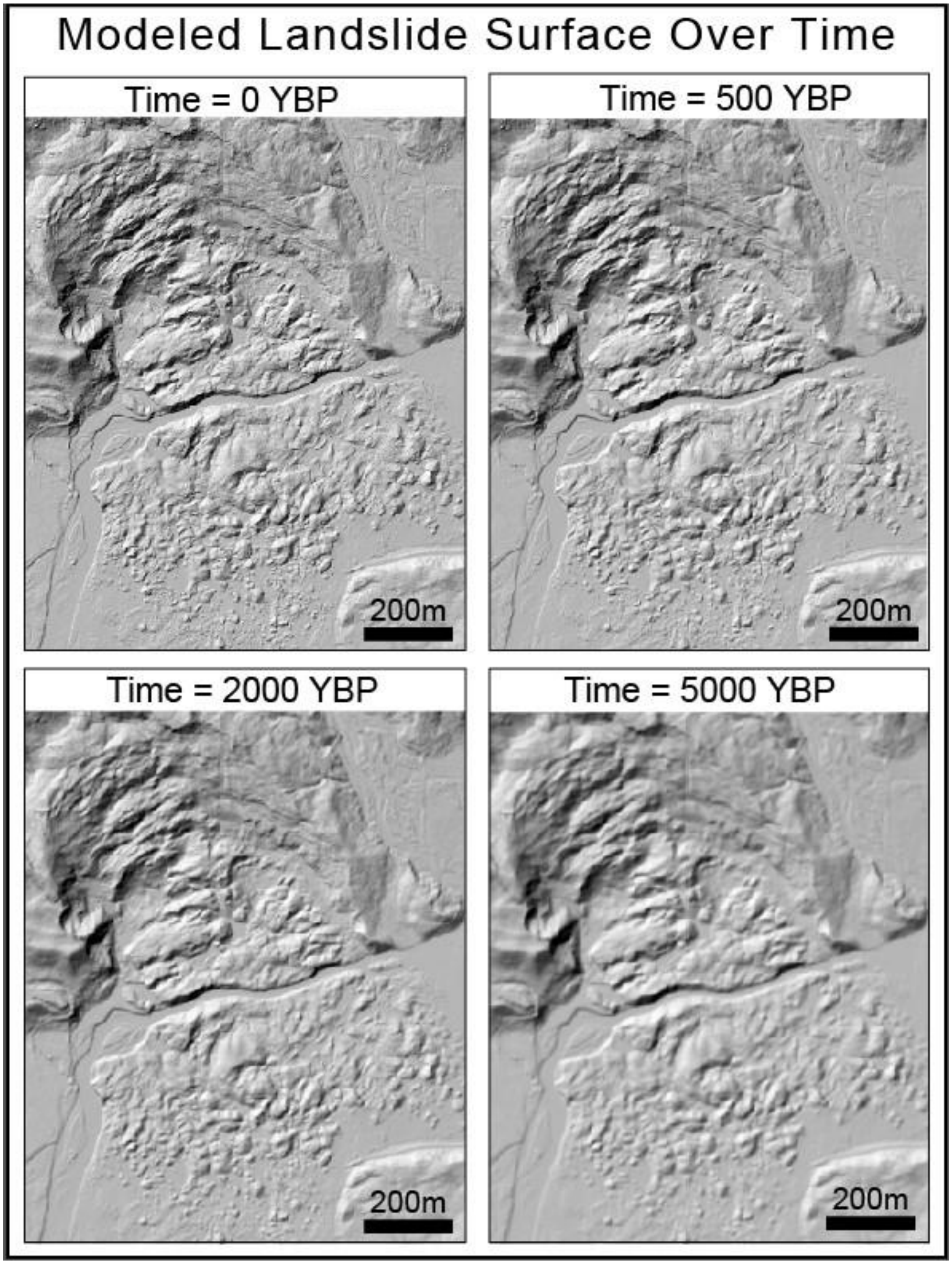

Figure 2.5. Hillshade images showing the modeled evolution of the Oso Landslide surface topography at time 0 years, 500 years, 2000 years, and 5000 years.

Supplementary References

Keaton, J. R., et al., 2014, The 22 March 2014 Oso Landslide, Snohomish County, Washington. Geotechnical Extreme Events Reconnaissance Association Report **GEER-036**.

Press, W. H., 2007, *Numerical recipes 3rd edition: The Art of Scientific Computing*. Cambridge University Press.

Ramsey, C. B., 2009, Bayesian analysis of radiocarbon dates. *Radiocarbon* **51,** 337-360.

Washington State Department of Transportation, 2014, Oso Landslide/Stillaguamish River LiDAR. Puget Sound LiDAR Consortium.

Chapter 3. RAINFALL TRIGGERS MORE DEEP-SEATED LANDSLIDES THAN CASCADIA EARTHQUAKES IN THE OREGON COAST RANGE, USA[2]

The coastal Pacific Northwest USA hosts thousands of deep-seated landslides. Historic landslides have primarily been triggered by rainfall, but the region is also prone to large earthquakes from the 1,100km-long Cascadia Subduction Zone megathrust. Little is known about the number of landslides triggered by these earthquakes because the last magnitude 9 rupture occurred in 1700 CE. Here we map 9,938 deep-seated bedrock landslides in the Oregon Coast Range and use surface roughness dating to estimate landslide age. By analyzing observed and simulated landslide frequency, we find that past earthquakes triggered no more than a few hundred landslides per event, accounting for less than half of the landslides in the last 1,000 years. These results agree with findings from other recent subduction-zone earthquakes where few coherent landslides were mapped. Our results suggest that, despite its proximity to the megathrust, most deep-seated landslides in the Oregon Coast Range were triggered by rainfall.

3.1 INTRODUCTION

Landslides are one of the most significant secondary hazards of large earthquakes. Hillslope failures triggered by shaking can impact homes and infrastructure, dam rivers, and cause flooding, sometimes in catastrophic outbursts (Costa & Schuster, 1988; Yin et al., 2009; Petley, 2012; Fan et al., 2019). In the Pacific Northwest of the United States, magnitude 8-9 earthquakes occur every 300-500 years along the Cascadia Subduction Zone (CSZ) (Goldfinger

---

[2] Manuscript in preparation for submission for *Sciences Advances*, with authors S. R. LaHusen, A. R. Duvall, A. M. Booth, A. Grant, B. A. Mishkin, D. R. Montgomery, W. Struble, J. J. Roering, and J. Wartman

et al., 2012), a 1,100km long megathrust fault that accommodates subduction of the Juan de Fuca plate beneath the North American plate (Figure 3.1). Empirical estimates for the number of triggered landslides for earthquakes of this magnitude range from 50,000-1,000,000+ (Keefer, 1984; Malamud et al., 2004; Marc et al., 2016), representing a risk to the millions of people living in the region. However, the few complete coseismic landslide inventories in subduction zones challenge assumptions about the number and location of landslides triggered by such earthquakes. Only 1,226 landslides were mapped following the 2010 M8.8 Maule Earthquake in Chile (Serey et al., 2019). The following year, the M_w9.0 Tohoku earthquake struck Japan, causing widespread damage but resulting in just 3,477 mapped landslides (Wartman et al., 2013). Most of the landslides triggered in both earthquakes were shallow, disrupted slides (defined here as landslides where the mobilized slide material mostly or entirely disintegrates during failure, resulting in flow or avalanche style behavior) and lateral spreads. In Cascadia, the timing of the last great CSZ earthquake is well constrained to 1700 CE (Atwater, 2005), yet no prehistoric landslides have been directly dated to that time (Perkins et al., 2018). Recent landslide dating efforts have precisely determined the age of several landslide dammed lakes in western Oregon, but none date to 1700 CE (Struble et al., in press). Complicating the search for past coseismic landslides in Cascadia is the characteristically wet climate of the Pacific Northwest, where heavy rainfall often triggers landslides (Chleborad, 2003; Turner et al., 2010; Wartman et al., 2016). The challenge of parsing the relative importance of these triggers is essential to understanding what controls landslide hazards and, on longer timescales, landscape denudation in the region.

One significant barrier to understanding the behavior and triggering mechanisms of past landslides is the difficulty of dating landslides on a regional scale. Landslide mapping inventories, however accurate, are limited in their ability to assess landslide triggering or event frequency because they often contain no age information for individual slope-failure events. Recent work in Washington State has shown that for landslides in glacial sediment, surface roughness measured from lidar data can be used as a proxy for landslide age, enabling regional landslide chronologies to be constructed from a limited set of absolute dates (LaHusen et al., 2016; Booth et al., 2017). This technique takes advantage of the topographic smoothing of landslide deposits over time as weathering, erosion, and soil transport moves material from convex areas to concave areas. Thus far, this technique has been applied to Quaternary glacial deposits, and here we demonstrate its effectiveness in dating bedrock landslides.

In this study, we apply surface roughness dating to a new inventory of 9,938 manually mapped, deep-seated bedrock landslides across 15,000 km^2 in the sandstones and siltstones of the Tyee and Elkton Formations of the central Oregon Coast Range (OCR) (Figure 3.2). The OCR, a mountainous swath of western Cascadia, has a well-documented abundance of prehistoric and historic landslides, and is prone to both deep-seated bedrock landslides and shallow translational slides and debris flows (Baldwin, 1958; Lane, 1987; Montgomery et al., 2000; Roering et al., 2005, Hammond et al., 2009). Thousands of landslides have previously been identified in the OCR (Burns, 2017; Burns et al., 2012), and automated landslide identification techniques suggest up to 25% of the Tyee Formation is affected by deep-seated slides, underscoring the importance of this process to landscape evolution and morphology (Roering et al., 2005). Valley-spanning prehistoric landslides exist throughout the region, with remnant portions of deposits causing substantial upstream aggradation (Lane, 1987). Historic deep-seated landslides include a failure that occurred in 1975, damming Drift Creek and creating a lake that persists today.

Numerical earthquake models suggest the OCR, which overlies the CSZ and in some places is less than 100km from the associated offshore trench, may experience peak ground accelerations >0.6g during magnitude 9 earthquakes (Frankel et al., 2018, Wirth et al., 2018; Figure 3.1). Despite this proximity to the megathrust, the lack of historic records of coseismic landslides associated with the CSZ inhibits our understanding of where and how slopes fail during these large earthquakes. With the recent availability of <1m resolution bare-earth lidar coverage of the entire OCR, far more accurate and complete landslide mapping is now possible, as are surface roughness dating techniques that require high-resolution topographic data. Using 14 bedrock landslides with independent age constraints ranging from <10 to >40,000 years before 2019 (ybp) from this and other studies, we find an exponential relationship between landslide deposit surface roughness and age. We then use a calibrated roughness-age function to estimate the ages of all mapped landslides in the study area and examine trends in landslide frequency over the past 1,000 years to determine the importance of past large earthquakes as landslide triggers.

3.2 RESULTS

Surface Roughness Dating of Bedrock Landslides

Previous work has tested the ability of numerous roughness metrics to both track known landslide ages and correctly identify relative ages between landslides with cross-cutting relationships (Booth et al., 2017). For this study, we adopt the measure with the highest combined performance from these previous tests: the 2-D continuous wavelet transform (CWT). We performed the CWT using a Mexican Hat wavelet at a 20m spatial scale on 0.9m – 1m resolution lidar bare-earth elevation data, which is equivalent to calculating topographic curvature (the Laplacian of elevation) at the specified length scale (Lashermes et al., 2007). We take the mean magnitude of the wavelet coefficient from the 14 mapped landslide polygons of known age to represent their roughness (Table S1, Figure S1). Similar to previous work in Washington State, the relationship between landslide deposit roughness and age is well fit by an exponential decay function. We fit a robust (least absolute error) exponential regression using these roughness-age data, which resulted in less systematic overprediction in the younger portion of the dataset than a least-squares regression (Figure 3.3. We use this function to estimate the ages and uncertainties of all 9,938 landslides across the study area based on their measured roughness value (Figure 2B). As a conservative estimate of uncertainty for any single estimated landslide age, we calculate prediction bounds at a 95% confidence level for all age values. Uncertainty in predicted ages increases with time. For landslides estimated to be historic, 95% prediction bounds yield an age range of 0-1,300 years. This age range grows to 0-2,400 years for landslides estimated to be 1,000 years old. For landslides estimated to be thousands to tens of thousands of years old, uncertainty is plus or minus a few thousand years. While this technique is therefore not appropriate for pinpointing the exact triggering time for an individual slope failure, it offers sufficient accuracy to examine broad-scale landsliding patterns in space and time across a landscape when applied to large landslide inventories.

Estimating Landslide Frequency through Time in the Central Oregon Coast Range

The predominant pattern in landslide frequency within the study area is an apparent non-linear decrease in frequency with age (Figure 3.4A). This same pattern was observed in previous landslide chronologies (LaHusen et al., 2016, Booth et al., 2017), and likely reflects both a real preservation bias of young slides, and a bias effect associated with using an exponential function to estimate age (Supplementary Materials). The preservation bias should be expected as ongoing hillslope and fluvial processes tend to reshape relict landslide deposits, and as old slides are reactivated. Equilibrium hillslope adjustment timescales calibrated to the OCR suggest the topographic signature of the deepest landslides in the study area may only persist for tens of thousands of years after failure, while the legacy of smaller, shallower landslides is even more short-lived.

Together, these processes lead to a preservation bias toward younger landslides, consistent with the well-documented apparent decline of sedimentation and erosion rates with geologic age that has been attributed to biased representation of the geologic record (Schumer & Jerolmack, 2009). As a result, we cannot compare directly the true frequency of landsliding from tens of thousands of years ago to present day, but we can statistically identify peaks in the landslide age-frequency data that differ significantly from the background trend and may represent periods of widespread landslide triggering due to extreme storms or large earthquakes, for example. To test whether there is a signal from past CSZ earthquakes in the distribution of landslide ages, we focus on the age-frequency data for the last 1,000 years, where the on-shore and off-shore geologic record suggest three full-length (~M8.7 – 9.1) CSZ ruptures have occurred (Goldfinger et al., 2012), including the most recent 1700 CE earthquake. After selecting a subset of 2,676 landslides with estimated ages <1,000 years, we bin landslide frequency into twenty 50-year intervals and then estimate slide frequency per year for each bin (Figure 3.4B).

Landslide frequency over the last 1,000 years reveals a non-linear increase in landslide frequency towards the present, consistent with the overall trend observed for the last ~50,000 years. Superimposed on this trend are two sharp peaks at 125 ybp and 225 ybp, and a broad peak centered at 375 ybp (Figure 3.4B). To test whether these peaks represent noise in the dataset or a real increase in landslide frequency at these times, we compare this best-fit frequency plot with a suite of frequency plots generated from a bootstrap analysis. This bootstrap analysis allows the roughness and age values for landslides of known age to vary within their uncertainties, then fits a unique regression for each of 10^4 bootstrap runs. This accounts for error in our landslide frequency plots caused by uncertainty in the roughness-age data used to fit the exponential regression we use to date each landslide. When we plot the bootstrapped mean frequency as well as the lower 5th and upper 95th percentiles, a trend of decreasing frequency with age is observed, similar to the frequency plot generated by the best-fit regression; however, no peaks appear in the bootstrap mean distribution. When individual frequency plots from the bootstrap analysis are examined, peaks of similar amplitude as the peaks observed in the best-fit frequency plot appear at random times in the 1,000-year history. Collectively, this analysis suggests that the sharp peaks observed in the best-fit frequency plot may not be statistically significant, and thus deviations from a constant rate of landsliding during the last 1,000 years should be viewed with caution.

Quantifying Coseismic Landslide Triggering Rates from CSZ Earthquakes

Although we cannot detect clustered landslide activity in our analysis, the overall shape of the curve is useful in determining the relative importance of earthquakes as a triggering mechanism in the OCR. Because of the large uncertainty in the roughness-age technique, pulses of coseismic landslides may not show up as discrete peaks in the resulting landsliding frequency data but could form broad undulations which control the overall shape of the dataset over the last 1,000 years. Moreover, there has not been a large earthquake in Cascadia for 319 years, so we may expect that the frequency plot from a landslide inventory triggered primarily by earthquakes would peak around the time of the 1700 CE earthquake and decrease towards present-day. To systematically explore these scenarios and to place bounds on the number of possible earthquake-triggered landslides in the last 1,000 years, we generated simulated landslide chronologies and compared those to the observed landslide dataset. By superimposing pulses of coseismic landslides during times of large CSZ earthquakes on a specified background rate of landsliding, we compared modeled frequency plots for a range of hypothetical landslide histories. These modeled datasets help to account for the uncertainty in the roughness-age dating method that arises from natural variability in roughness values for landslides of the same age, thus providing a statistically justified way of interpreting our observed frequency data. Simulated landslide chronologies allow us to discern what the frequency plots for the last 1,000 years should look like if: 1. All landslides are seismically triggered, 2. All landslides are triggered by background processes (we assume rainfall as the predominant background trigger) or 3. A mix of seismic and rainfall triggered landslides.

The simulated landslide history composed entirely of ‘background’ landslides, where no coseismic landslide pulses are added most closely follows the observed frequency plot (Figure 3.5A). For this ‘purely background’ simulated history, the observed data falls almost entirely within the 5th and 95th percentile bounds of the model runs. As we increase the number of slides that are triggered in each earthquake pulse in the simulated landslide histories, the resulting frequency plots deviate further from the observed data. In model runs where 50% of the total landslides are coseismic, corresponding to 600 landslides triggered per earthquake, the observed data falls outside the modeled bounds for two distinct intervals in the 1,000 year history: from ~700-250 ybp and from ~150 ybp to present (Figure 3.5B). The purely coseismic simulated history, for which 1,300 landslides are triggered per earthquake, reveals the strongest deviation from the observed frequency data, with minimal overlap between simulated and observed landslide frequency (Figure 3.5C). Even in the 100% coseismic simulation, the discrepancy between observed and simulated frequencies is caused by a shift in the overall shape of the curve, not by the formation of distinct frequency peaks at the times of earthquakes. The diffuse nature of these peaks cause them to overlap such that they are indiscernible. This effect is due to both natural variability in initial roughness conditions immediately after slope failure and variability in the quality of lidar data used to measure roughness, which together result in a distribution of roughness values for landslides of the same age. When we shorten the bandwidth of this roughness distribution by decreasing the standard deviation (SD) of roughness values used in the model runs, frequency peaks do appear (Figure S2). However, this requires unrealistic SD values, which are substantially lower than the measured SD, and much lower than the more conservative SD we adopt for all model runs (see materials and methods).

3.3 DISCUSSION

In this study, we demonstrate that roughness dating of landslide deposits can be applied to large inventories of deep-seated bedrock landslides. In conjunction with previous studies of landslides in glacial sediments, this work suggests roughness dating is a broadly applicable tool suitable for use in diverse landscapes underlain by either bedrock or Quaternary sedimentary deposits (LaHusen et al., 2016, Booth et al., 2017). In the Tyee Formation of the OCR, we show roughness dating to be a powerful tool for rapidly estimating the ages of nearly 10,000 landslides across 15,000 km^2, albeit with less accuracy than traditional landslide geochronometers such as radiocarbon dating. While this uncertainty may be too high to identify peaks in landslide frequency associated with individual earthquakes that occur every few hundred years in this region, the technique does offer an unprecedented means of parsing the relative importance of coseismic landslide triggering versus other triggering mechanisms.

Because there has not been a large earthquake in the region in over 300 years, the shape of the observed versus modeled landslide frequency plots differ substantially, with frequency dropping off rapidly toward the present in simulated landslide histories that incorporate a larger relative proportion of coseismic landslides. The observed landslide frequency over the last 1,000 years shows the opposite: a slight increase in landslide frequency towards present day. Some of this increase is likely due to preservation bias, though we cannot discount the possibility of a real landslide frequency increase, potentially driven by widespread logging beginning in the late 19th century. The observed frequency is best reproduced with modeled simulations that include no pulses of coseismic landslides during the times of great CSZ earthquakes. In simulations where coseismic landslides account for half of the total landslides, the modeled frequency through time deviates substantially enough from the observed frequency that these simulations likely represent a conservative bound on the maximum proportion of coseismic triggering: equivalent to no more than 600 landslides per earthquake event.

The apparent dearth of coseismic landslides in the study area may be surprising, given the proximity of the region to the CSZ megathrust and the intense ground shaking predicted by numerical earthquake simulation models (Frankel et al., 2018, Wirth et al., 2018). However, these results are consistent with the conclusions drawn from recent coseismic landslide inventories mapped after subduction zone earthquakes in Maule, Chile (Serey et al., 2019) and Tohoku, Japan (Wartman et al., 2013). These studies found the total number of coseismic landslides fell 1-2 orders of magnitude short of expected values based on earthquake magnitude–landslide frequency scaling relationships developed for crustal faults (Malamud, 2004; Marc et al., 2016). Moreover, coherent, deep-seated landslides made up the smallest number of landslides per failure style in the mapped inventories. Of the 1,226 landslides Serey et al. (2019) mapped after the Maule earthquake, only 8 were identified as coherent, deep-seated landslides.

While deep-seated landslides are large and may be very destructive, smaller debris flows or shallow translational landslides may be expected to occur in far greater number, based on both landslide area-frequency scaling relationships (Malamud, 2004; Marc et al., 2016) and recent subduction zone earthquake-triggered landslide inventories (Wartman et al., 2013; Serey et al., 2019). These processes have been shown to be particularly prevalent in steep catchments in the central OCR (Benda, 1990), and, importantly, could represent the dominant style of coseismic landslide in the study area. By its nature, our methodology does not account for shallow failure styles. Shallow landslides and debris flows do not often leave a lasting impression on the landscape. Colluvial hollows, a common debris flow source, refill with hillslope material, and shallow landslide deposits are less voluminous and more easily evacuated (Dietrich et al., 1982). This makes identifying and mapping these landforms difficult or impossible hundreds of years after the last large earthquake. In contrast, scars and deposits associated with deep-seated landslides may last tens of thousands of years, a timespan that may encompass dozens or even hundreds of earthquakes in seismically active regions.

Given the well-established importance of rainfall as a landslide trigger (Caine, 1980; Van Asch et al., 1999; Froude & Petley, 2018), the characteristically wet climate of the OCR, and the lack of evidence for seismic triggering of deep-seated landslides, we propose that precipitation likely triggers the majority of landslides in the study area. This conclusion is bolstered by recent efforts to pinpoint the timing of individual landslide deposits in the OCR using dendrochronology, often yielding ages with uncertainties of less than 1 year (Struble et al., in press). This ongoing work has revealed multiple deep-seated landslides that date to 1890 CE, when historical records indicate severe flooding in the region (Struble et al., 2019), but has not identified any 1700 CE coseismic landslides. Together, both methods converge on a similar dearth of 1700 deep-seated landslides and support the conclusion that the primary hazard posed by these types of landslides in Cascadia is driven by rainfall rather than large-magnitude subduction zone earthquakes.

3.4 MATERIALS AND METHODS

Landslide Mapping and Dating

To construct a surface-roughness age relationship, we mapped 9,938 deep-seated landslides in the Tyee Formation and overlying Elkton Formation. Because surface roughness dating requires the assumption that landslides smooth over time due to erosion and soil diffusion, landslide deposit polygons had to be mapped carefully to avoid headscarps, incised stream gullies, and river cutbanks. Mapping was completed manually using bare-earth lidar derived hillshade and slope images. Only the presently intact surfaces of landslide deposits were mapped in order to capture areas dominated by diffusive smoothing processes. Major roads and anthropogenic structures were removed from polygons before roughness was calculated (Figure S1).

We mapped only coherent rotational and translational deep-seated landslide deposits with areas of at least $5*10^3$ m^2 and with at least one dimension over 100m. In this study, we define coherent landslides as slope failures where the mobilized material has not completely disintegrated to the point of allowing flow or avalanche style runout. Coherent slides more consistently preserve roughness elements like intact blocks, minor scarps, hummocks, and compressional ridges needed for roughness dating. Wherever remobilized portions of older landslide deposits satisfying these criteria were observed, they were mapped as individual slides. To satisfy the assumption inherent to surface roughness dating that all landslides fall within a range of expected initial roughness values directly after they occur, certain failure modes were excluded from the analysis. Landslides with channelized travel paths, debris flows, and earthflows were not considered, as the mechanics of these landslide types do not universally produce classic deep-seated landslide morphologies such as hummocky topography, scarps, and displaced blocks characterized by high initial roughness, as is typical of coherent landslides.

A suite of landslides with independently constrained ages is necessary for roughness-age dating, as these landslides provide the data to regress against roughness to define the roughness-age function used to estimate the ages of other landslides in the study area. We employed radiocarbon dating and historical repeat aerial imagery to ascertain the timing of failure for six landslides in the mapped chronology (Table S1). In addition, we used dates from previous work, including recent dendrochronology dating, for 8 other landslides (Struble et al., 2019; Richardson, 2018; Burns, 2017; Hammond et al., 2009; Worona & Whitlock, 1995; Lane, 1987; Baldwin, 1958) yielding a total dataset of 14 landslides of known age (Table S1). Because we date multiple landslides younger than 1950 CE, we report dated landslide ages in this study as years before 2019, as opposed to the radiocarbon convention of years before 1950. In this manuscript, we use the phrase ‘years before present’ and its abbreviation ‘ybp’ to mean years before 2019.

Surface Roughness Analysis and Landslide Age Estimation

For roughness dating to be applicable to a landslide-prone region, the initial roughness of landslide deposits is assumed to be similar, falling within a range of relatively high expected values. An additional assumption is that the material properties of the landslide and the climate of the study area are both similar enough that the rate of erosion and soil diffusion does not vary dramatically between landslides within the inventory. Moreover, while this technique has been shown to be applicable to many landslides across large study areas (Booth et al., 2017), it has not yet been implemented on bedrock landslides. To test the utility of the approach on bedrock landslides, we focus our efforts on a swath of the Central Oregon Coast Range, underlain entirely by Eocene marine sedimentary rock of the Tyee and overlying Elkton formations.

We measured the roughness of each mapped landslide using the 2D CWT with a Mexican Hat wavelet (Figure S1), which is defined as the 2nd derivative of the Gaussian function (Lashermes et al., 2007). We first calculated the CWT at spatial scales of 4m, 15m, 20m, and 45m to find the scale which offered the best-fit to the landslides of known age. For each CWT analysis, roughness values were computed for each cell in the 0.9m DEM, and mean values for each landslide deposit of known age were extracted from mapped polygons and used to plot age against roughness. Two regression methods, robust (least absolute error or L1-norm) and least-squares (L2 norm), were used to fit single exponential functions to these roughness-age datasets. We tested the performance of both methods in fitting the entire age range of dated landslides as well as a subset of young landslides (<1,000 ybp). It was important to select a fit that did not result in a systematic overprediction or underprediction in age estimations for the youngest landslides, as we used this fit to examine frequency trends in the last 1,000 years. When the entire range of ages in the dataset was considered, the standard error (SE) of the least-squares regression was slightly lower ($\sim 1.2 * 10^3$ years) compared to the robust regression ($\sim 1.6 * 10^3$ years). The least-squares regression optimized the fit for the oldest (>40,000 ybp) landslides, but systematically overestimated the ages of the younger landslide data points. When just the ten landslides less than 1,000 ybp were considered, the least-squares regression resulted in nearly double the SE as the robust regression: ~400 years versus ~200 years, and examination of residual plots showed less bias in the robust regression. Because the robust regression method is less sensitive to outliers than the least-squares regression, it most effectively fits a function across the age range of the dataset, especially for the younger (<1,000 ybp) landslides. This robust regression, which we deem the best-fit to our observed data, yields the following function which we use to estimate landslide age across the study area: $t = 1.428 \text{ x } 10^6 \; * \; e^{-125.8R}$, where t = estimated landslide age, in years before 2019, and R is the average magnitude of the wavelet coefficient at a 20m length scale within a mapped landslide polygon, m^{-1} (Figure 3.3.

Simulated Coseismic Landslide Chronologies

If large CSZ earthquakes do periodically trigger widespread landsliding in the study area, we would expect the resultant peaks in the histogram to be diffuse rather than sharp, due to the variability of measured roughness values within each pulse of coseismic landslides. To account for this variability, and to aid in a more robust interpretation of the observed landslide frequency data, we generated simulated landslide chronologies. These simulated chronologies offer a means to estimate the proportion of landslides in the study area triggered by large CSZ earthquakes. Specifically, they allow us to better determine what how a coseismic signal should look. By comparing the observed and synthetic datasets, we can also deduce whether the apparent steady increase in landslide frequency we observe could be due to uncertainty in the roughness dating technique.

We assume that when a pulse of landslides occurs, such as from a large earthquake, landslides fail instantaneously, and their deposits have normally distributed roughness values. Over time, both the mean and the standard deviation (SD) of the roughness values that compose this pulse decreases. The SD decreases because the roughest landslides have more regions of high curvature, and therefore smooth considerably faster than the landslides with lower initial roughness, effectively shrinking the distribution. This has been demonstrated numerically (Booth et al., 2017) and is supported by both geomorphic transport laws (Roering et al., 1999) and the exponential form of the roughness-age regression itself. To calculate the SD of roughness values for a specific age, a dataset of landslides of known age would ideally include many landslides of the same age. From our landslides with known ages, we calculate the SD for 4 landslides with ages that fall within 100 years of the 1700 CE earthquake, yielding a value of $2.8*10^{-3}$ m^{-1}. However, to address the uncertainty in calculating the SD from a small sample, we chose to double the measured SD and instead use a SD of $5.6*10^{-3}$ for all modeled landslide distributions. Rather than attempt to scale down SD with age, we take a conservative approach to this uncertainty and use the same value for all the entire 1,000-year simulation. We acknowledge that the modeled roughness SD has a substantial effect on the resulting landslide frequency plots. Very high SD values yield estimated ages that are skewed towards present day, producing a steep non-linear increase in apparent frequency towards present day. However, this does not occur until SD values exceed $1.1*10^{-2}$, a value 4 times greater than that measured in the study area for landslides ~ 1700 CE (SM, Figure S2).

Simulated landslide chronologies consist of two components: a background rate of sliding and pulses of coseismic landslides. To build these chronologies, we first generate ten coseismic landslide pulses at the times of past widespread turbidite events T1 (1700 CE) – T10. These widespread turbidite triggering events, identified by Goldfinger et al. (2012), are thought to correspond to past, full-length CSZ ruptures with estimated magnitudes of 8.7-9.1. The number of landslides triggered during each earthquake can be adjusted, allowing for any proportion of coseismic landsliding to be examined. Next, we prescribe an adjusted background rate of landsliding, in slides/year. This represents a spatial and temporal average across the entire study area of the rate of non-seismic landslide occurrence per year for the last 5,000 years. Although we specifically examine landslide frequency over the last 1,000 years, we extend the simulated chronology to 5,000 ybp to eliminate any effects from old landslides with erroneously young estimated ages. At each timestep in the chronology, a randomly generated, normally distributed set of landslide roughness values corresponding to the timestep age is added. The background rate is constant for each model run but is scaled depending on the number of coseismic landslides triggered in earthquake pulses so that, after adjusting for preservation bias, the total number of simulated landslides estimated to have ages of less than 1,000 ybp is equal to the total number observed: ~2,700 landslides. Because of the error associated with converting a roughness value to an age, coseismic landslide pulses have tails that extend past 1,000 ybp, so the prescribed total number of coseismic landslides triggered by the 3 large earthquakes in the last 1,000 years is greater than the total number estimated to be less than 1,000 ybp. For example, for the simulated 50% coseismic landsliding scenario, 600 coseismic landslides are prescribed per earthquake for a total of 1,800 coseismic landslides in the last 1,000 years, while only 1,317 are estimated to have ages less than 1,000 ybp (Figure 3.5B). Finally, to account for the preservation bias in the observed frequency, the total number of landslides for each simulated chronology is scaled as a function of time. We adopt a normalized exponential fit to the observed frequency data as this scaling function. This allows for a direct comparison between simulated and observed frequency plots.

In this paper, we show results from simulations of 0% coseismic triggering, 50% coseismic triggering, and 100% coseismic triggering, corresponding to 0, 600, and 1300 coseismic landslides triggered per CSZ earthquake, respectively. Each of these three sets of conditions are modeled 10^4 times, then the ages are calculated for each run using the same best-fit roughness-age regression used to calculate observed ages. Lastly, the mean frequency, as well as 5th and 95th bounding percentiles, for all model runs are calculated and plotted (Figure 3.5).

Statistical Analysis of Age Estimates and Sources of Uncertainty

The total error in our estimated landslide ages stems from natural variability in initial roughness conditions, uncertainty in roughness calculations, uncertainty in interpreting radiocarbon-based landslide ages, and the inherently subjective nature of mapping landslides by eye. We attribute most of the uncertainty in our surface roughness calculations to variations in ground point density from the lidar point clouds used to generate the digital elevation models used in this study, an effect that has been noted in previous work (Burns et al., 2010). To quantify this effect and assign error bars to points on the roughness-age curve, we compare the roughness of two lidar datasets taken in 2011 and 2015 of the same region within the Oregon Coast Range (Supplementary Materials). We assign the $\pm 2\sigma$ m^{-1} of the observed error between repeat lidar datasets ($3.15*10^{-3}$) as the $\pm 2\sigma$ m^{-1} for each point used in our roughness-age regression and plot this value as horizontal error bars on landslides of known age (Figure 3.3.

Because our age estimations are determined by the parameters of the best-fit regression, we needed to account for uncertainty in the regression itself. Uncertainty in the regression would primarily arise from uncertainty in the roughness-age data points used in the fitting process. To address the effect of error in these, we employ a bootstrap analysis. For 10^4 runs, the roughness and age for each of the 14 landslides of known age were randomly selected at a frequency dependent on the respective uncertainty distribution for each landslide, and a best-fit exponential regression was fit. Each bootstrapped regression is then used to estimate landslide ages and generate landslide frequency versus time plots for both the measured roughness values in the study area and the roughness values generated in our simulated coseismic landslide datasets

(Figure 3.4). This allows us to interpret trends in our observed frequency in a more statistically robust manner..

3.5 FIGURES

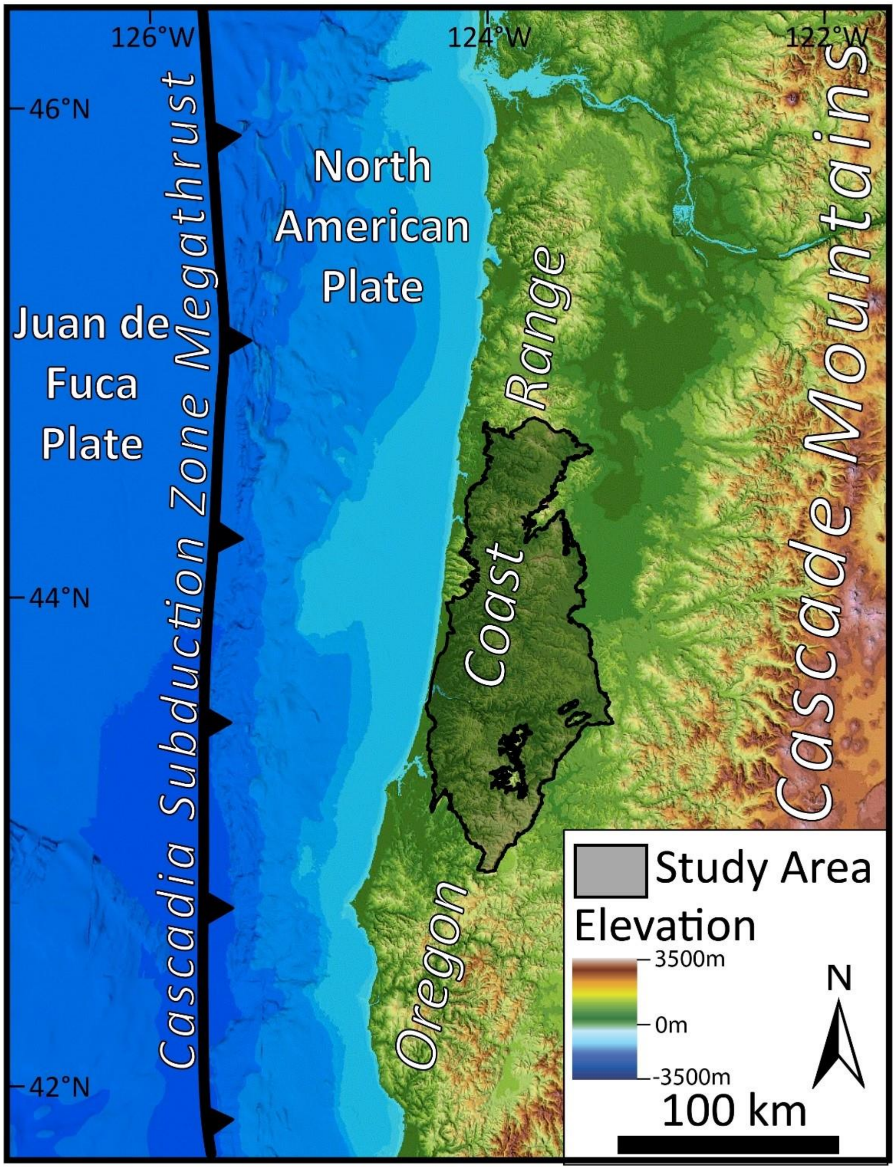

Figure 3.1. Tectonic setting and geography of study area. Black outline depicts the central Oregon Coast Range study area, which is underlain by the Eocene Tyee Formation and overlying Elkton Formation. The Cascadia Subduction Zone runs roughly N-S for over 1,100km just offshore. Shaded relief basemap compiled from USGS 30m elevation data and NOAA bathymetry by the State of Oregon.

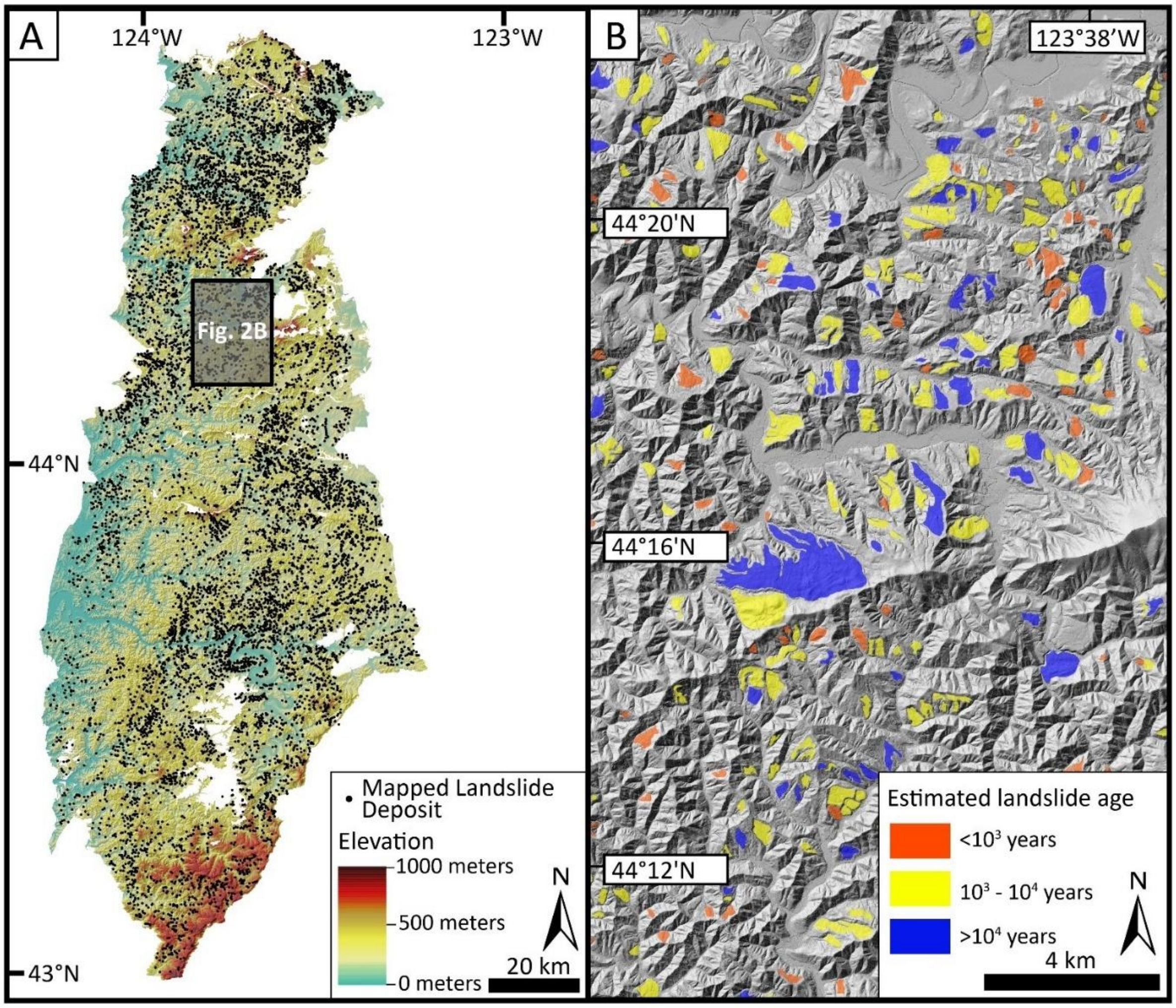

Figure 3.2. Landslide locations within the study area. (A) Manually mapped deep-seated landslide deposits (n = 9,938) from the study area (outline in Figure 3.1) shown as black circles over a base map of elevation and shaded relief. Inset map for Figure 3.2b outlined in black. (B) Detailed map of landslide deposits and estimated age ranges. Deep-seated landslides shown as polygons draped over 0.9-1.0 m bare-earth lidar derived hillshade, with estimated ages from deposit surface roughness identified by polygon color.

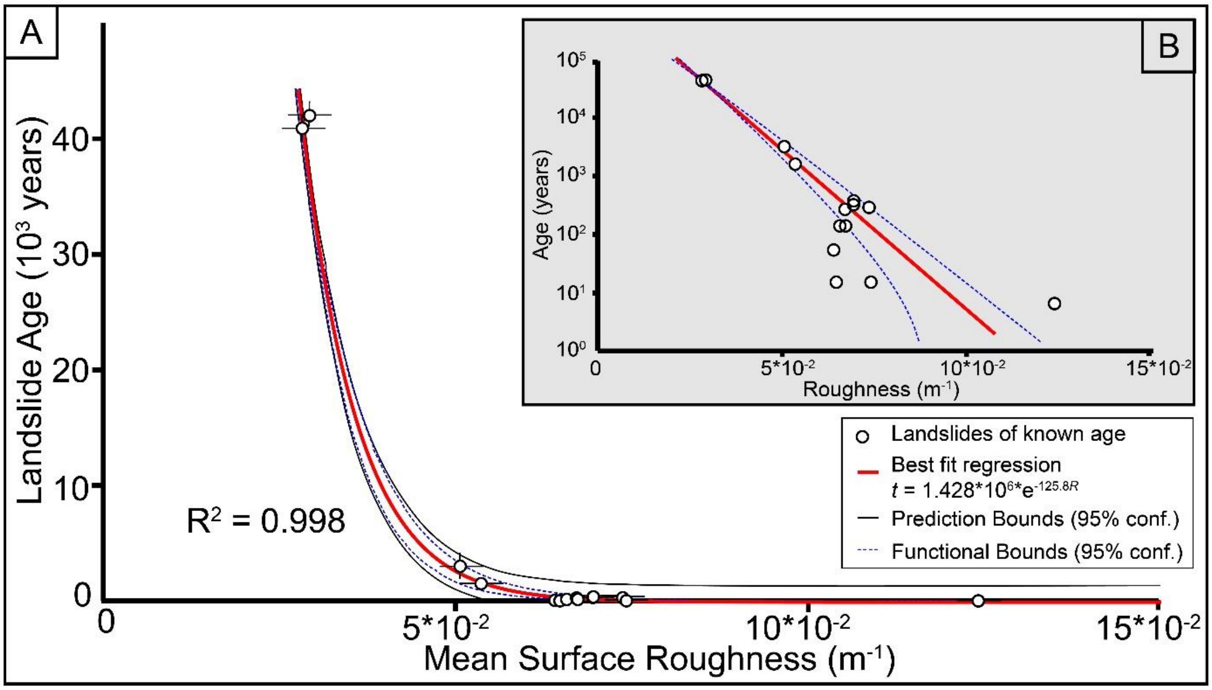

Figure 3.3. Plot of landslide age versus deposit surface roughness. (A) Open circles represent ages of landslides with independent timing constraints from radiocarbon, dendrochronology, or repeat aerial imagery plotted against the surface roughness of those deposits, quantified by the average magnitude of the wavelet coefficient for each polygon using a continuous wavelet transform with a 20m Mexican Hat Wavelet. Exponential decay function fit to these data shown as red line, where t = landslide age (years before 2019), R = landslide roughness (mean wavelet coefficient of mapped polygon). Functional bounds show 95% confidence of fitted regression, plotted as blue dashed lines. Prediction bounds show 95% confidence for landslide age prediction, plotted as solid black lines. (B) The same data points and regression plotted on a semilog axis to better illustrate variability in landslide ages for slides less than 10^3 years old.

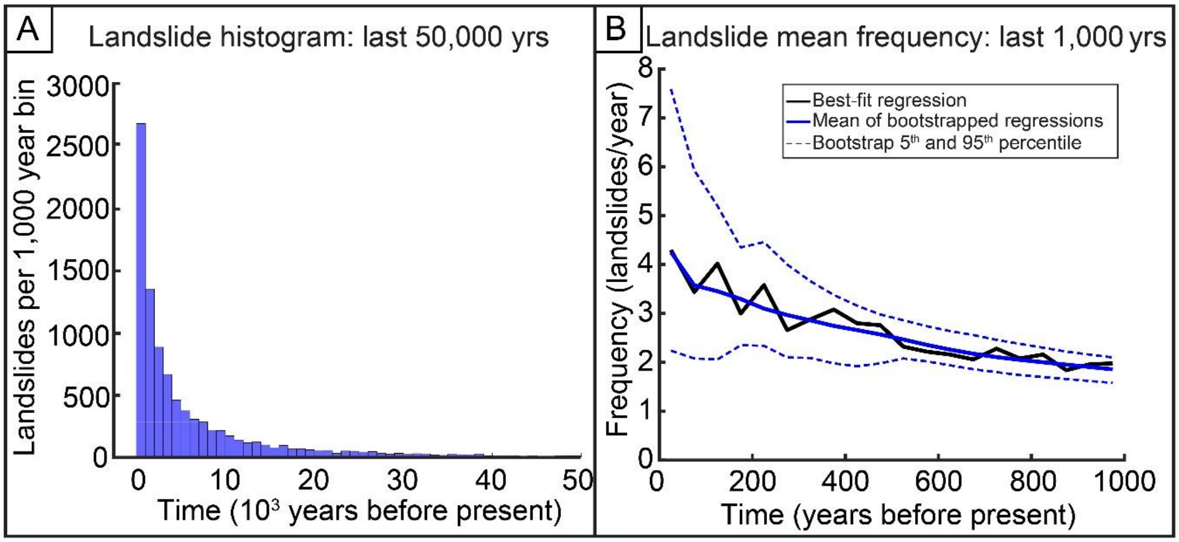

Figure 3.4. Distribution of landslide ages and estimated landslide frequency. (A) Histogram of landslide ages for the last 50,000 years across the study area show a non-linear decrease with time which is likely the result of the preservation bias of younger landslide deposits. (B) Mean yearly landslide frequency estimated for the last 1,000 years. Frequency estimated from the best-fit roughness age regression is shown as solid black line. A bootstrap analysis of 10^4 possible roughness-age regressions fit to our data is shown in blue, where the solid line is the mean and the dashed lines are the lower 5th and upper 95th percentiles of the bootstrap analysis.

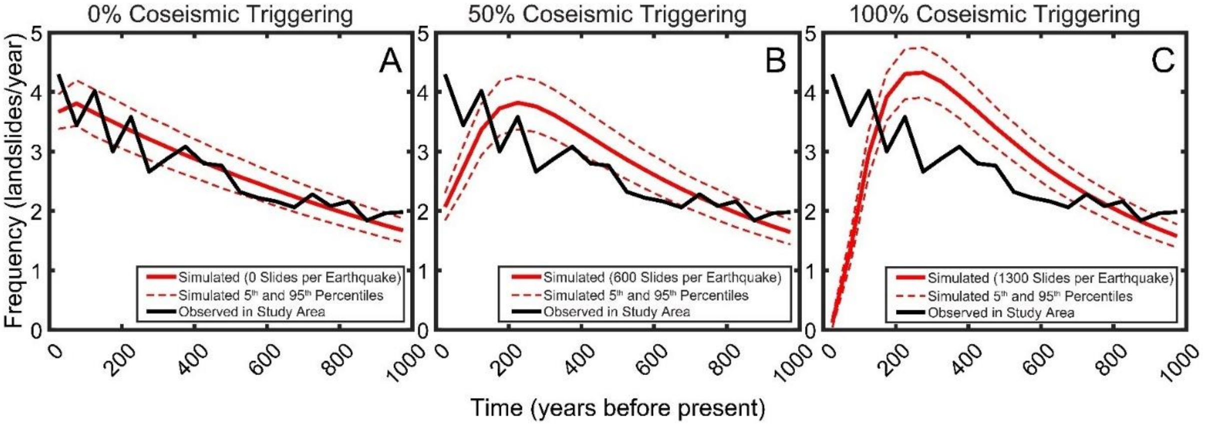

Figure 3.5. Comparison of observed versus simulated landslide frequency histories for the last 1,000 years. (A) Observed frequency calculated from age estimates for landslides mapped in the study area is plotted as a solid black line. Simulated landslide frequency for 10^4 modeled scenarios where no landslides are triggered during past full-rupture CSZ earthquakes is shown in red, where the solid line is the mean and the dashed lines are the lower 5th and upper 95th percentiles of all model runs. In the modeled scenarios, landslides are triggered at a steady rate (B) Observed frequency shown as solid black line, simulated landslide frequency shown in red for modeled scenarios where 50% of the total modeled landslides triggered by CSZ earthquakes, equivalent to 600 landslides per earthquake. The other 50% are triggered at a steady rate. (C) Observed frequency shown as solid black line, simulated landslide frequency shown in red for modeled scenarios where 100% of the total modeled landslides triggered by CSZ earthquakes, equivalent to 1300 landslides per earthquake.

3.6 CHAPTER 3 REFERENCES

Atwater, B.F., Musumi-Rokkaku, S., Satake, K., Tsuji, Y., Ueda, K., and Yamaguchi, D.K. The orphan tsunami of 1700—Japanese clues to a parent earthquake in North America, 2nd ed.: Seattle, University of Washington Press, U.S. Geological Survey Professional Paper 1707, 135 p. (2015).

Balco, G., Finnegan, N., Gendaszek, A., Stone, J. O., & Thompson, N. Erosional response to northward-propagating crustal thickening in the coastal ranges of the US Pacific Northwest. *American Journal of Science*, *313*(8), 790-806. (2013).

Baldwin, E. M. Landslide lakes in the Coast Range of Oregon: Geological Newsletter. *Geological Society of the Oregon Country*, *24*(4), 23-24. (1958).

Benda, L. (1990). The influence of debris flows on channels and valley floors in the Oregon Coast Range, USA. *Earth Surface Processes and Landforms*, *15*(5), 457-466.

Booth, A. M., LaHusen, S. R., Duvall, A. R., & Montgomery, D. R. (2017). Holocene history of deep-seated landsliding in the North Fork Stillaguamish River valley from surface roughness analysis, radiocarbon dating, and numerical landscape evolution modeling. *Journal of Geophysical Research: Earth Surface*, *122*(2), 456-472.

Burns, B. J., Serin, D., Jones, C. B., & English, J. T. (2012) Open-File Report O-12-07, Lidar data and landslide inventory maps of the North Fork Siuslaw River and Big Elk Creek watersheds, Lane, Lincoln, and Benton Counties, Oregon

Burns, W. J., Coe, J. A., Kaya, B. S., & Ma, L. (2010). Analysis of elevation changes detected from multi-temporal LiDAR surveys in forested landslide terrain in western Oregon. *Environmental & Engineering Geoscience*, *16*(4), 315-341.

Burns, W.J. (2017). Statewide Landslide Information Database for Oregon, release 3.4: Oregon Department of Geology and Mineral Industries, Web: http://www.oregongeology.org/sub/slido/

Chleborad, A. F. (2003). Preliminary evaluation of a precipitation threshold for anticipating the occurrence of landslides in the Seattle, Washington, Area. *US Geological Survey open-file report*, *3*(463), 39.

Costa, J. E., & Schuster, R. L. The formation and failure of natural dams. *Geological Society of America bulletin*, *100*(7), 1054-1068 (1988).

Dietrich, W. E., Dunne, T., Humphrey, N. F., & Reid, L. M. (1982). Construction of sediment budgets for drainage basins. *Sediment Budgets and Routing in Forested Drainage Basins: Proceedings of the Symposium; 31 May-1 June 1982; Corvallis, Oregon. Gen. Tech. Rep. PNW-141,* U.S. Forest Service, p. 5-23

Fan, X., Scaringi, G., Korup, O., West, J., van Westen, C. J., Tanyas, H., Hovius, N., Hales, T.C., Jibson, R.W., Allstadt, K. E., and Zhang, L. (2019). Earthquake‐Induced Chains of Geologic Hazards: Patterns, Mechanisms, and Impacts. *Reviews of Geophysics*

Frankel, A., Wirth, E., Marafi, N., Vidale, J., & Stephenson, W. (2018). Broadband synthetic seismograms for magnitude 9 earthquakes on the cascadia megathrust based on 3D simulations and stochastic synthetics, Part 1: Methodology and overall results. *Bulletin of the Seismological Society of America*, *108*(5A), 2347-2369.

Goldfinger, C., C. H. Nelson, A. E. Morey, J. E. Johnson, J. Patton, E. Karabanov, J. Gutiérrez–Pastor, A. T. Eriksson, E. Gràcia, G. Dunhill, R. J. Enkin, A. Dallimore, and T. Vallier (2012). Turbidite event history—Methods and implications for Holocene paleoseismicity of the Cascadia subduction zone, U.S. Geological Survey Professional Paper 1661–F

Hammond, C. M., Meier, D., & Beckstrand, D. (2009). Paleo-landslides in the Tyee Formation and highway construction, central Oregon Coast Range. *Geological Society of America Field Guide*, *15*, 481-494.

Keefer, D. K. (1984). Landslides caused by earthquakes. *Geological Society of America Bulletin*, *95*(4), 406-421.

LaHusen, S. R., Duvall, A. R., Booth, A. M., & Montgomery, D. R. (2016). Surface roughness dating of long-runout landslides near Oso, Washington (USA), reveals persistent postglacial hillslope instability. *Geology*, *44*(2), 111-114.

Lane, J.W., 1987, Relations between geology and mass movement features in a part of the East Fork Coquille River Watershed, Southern Coast Range, Oregon [M.S. thesis]: Corvallis, Oregon State University, 107 p.

Lashermes, B., Foufoula‐Georgiou, E., & Dietrich, W. E. (2007). Channel network extraction from high resolution topography using wavelets. *Geophysical Research Letters*, *34*(23).

Lovell, J. B. (1969). Tyee Formation: Undeformed turbidites and their lateral equivalents: Mineralogy and paleogeography. *Geological Society of America Bulletin*, *80*(1), 9-22.

Malamud, B. D., Turcotte, D. L., Guzzetti, F., & Reichenbach, P. (2004). Landslides, earthquakes, and erosion. *Earth and Planetary Science Letters*, *229*(1-2), 45-59.

Marc, O., Hovius, N., Meunier, P., Gorum, T., & Uchida, T. (2016). A seismologically consistent expression for the total area and volume of earthquake-triggered landsliding. *Journal of Geophysical Research: Earth Surface*, *121*(4), 640-663.

Montgomery, D. R., Schmidt, K. M., Greenberg, H. M., & Dietrich, W. E. (2000). Forest clearing and regional landsliding. *Geology*, *28*(4), 311-314.

Oregon Department of Geology and Mineral Industries (2008). Oregon Geology Fact Sheet: Landslide Hazards in Oregon. Web: https://www.oregongeology.org/pubs/fs/landslide-factsheet.pdf

Petley, D. (2012). Global patterns of loss of life from landslides. *Geology*, *40*(10), 927-930.

Perkins, J. P., J. J. Roering, W. J. Burns, W. Struble, B. A. Black, K. M. Schmidt, A. Duvall, and N. Calhoun (2018), Hunting for landslides from Cascadia’s great earthquakes, *Eos, 99*

Richardson, K. N. D., Hatten, J. A., & Wheatcroft, R. A. (2018). 1500 years of lake sedimentation due to fire, earthquakes, floods and land clearance in the Oregon Coast Range: geomorphic sensitivity to floods during timber harvest period. *Earth Surface Processes and Landforms*, *43*(7), 1496-1517.

Roering, J. J., Kirchner, J. W., & Dietrich, W. E. (1999). Evidence for nonlinear, diffusive sediment transport on hillslopes and implications for landscape morphology. *Water Resources Research*, *35*(3), 853-870.

Roering, J. J., Kirchner, J. W., & Dietrich, W. E. (2005). Characterizing structural and lithologic controls on deep-seated landsliding: Implications for topographic relief and landscape evolution in the Oregon Coast Range, USA. *Geological Society of America Bulletin*, *117*(5-6), 654-668.

Schumer, R., & Jerolmack, D. J. (2009). Real and apparent changes in sediment deposition rates through time. *Journal of Geophysical Research: Earth Surface*, *114*(F3).

Serey, A., Piñero-Feliciangeli, L., Sepúlveda, S. A., Poblete, F., Petley, D. N., and Murphy, W. (2019). Landslides induced by the 2010 Chile megathrust earthquake: a comprehensive inventory and correlations with geological and seismic factors. *Landslides*, *16*(6), 1153-1165.

Snavely, P. D., Wagner, H. C., & MacLeod, N. S. (1964). Rhythmic-bedded eugeosynclinal deposits of the Tyee formation, Oregon Coast Range. *Kansas Geological Survey Bulletin*, *169*, 461-480.

Struble, W., Roering, J., Black, B., Burns, W., Calhoun, N., Wetherell, L. (*in revision*). Dendrochronological Dating of Landslides in Western Oregon: Searching for Signals of the Cascadia 1700 AD Earthquake. *Geological Society of America Bulletin*.

Struble, W., Roering, J., Black, B., Burns, W., Calhoun, N., Wetherell, L., 2019. Temporal clustering of landslide-dammed lakes in western Oregon using dendrochronology. Geological Society of America Abstracts with Programs 51(4), doi: 10.1130/abs/2019CD-329423

Turner, T. R., Duke, S. D., Fransen, B. R., Reiter, M. L., Kroll, A. J., Ward, J. W., ... & Bilby, R. E. (2010). Landslide densities associated with rainfall, stand age, and topography on forested landscapes, southwestern Washington, USA. *Forest ecology and management*, *259*(12), 2233-2247.

Wartman, J., Dunham, L., Tiwari, B., & Pradel, D. (2013). Landslides in Eastern Honshu Induced by the 2011 Tohoku Earthquake Landslides in Eastern Honshu Induced by the 2011 Tohoku Earthquake. *Bulletin of the Seismological Society of America*, *103*(2B), 1503-1521.

Wartman, J., Montgomery, D. R., Anderson, S. A., Keaton, J. R., Benoît, J., dela Chapelle, J., & Gilbert, R. (2016). The 22 March 2014 Oso landslide, Washington, USA. *Geomorphology*, *253*, 275-288.

Wirth, E. A., Frankel, A. D., Marafi, N., Vidale, J. E., & Stephenson, W. J. (2018). Broadband synthetic seismograms for magnitude 9 earthquakes on the Cascadia megathrust based on 3D simulations and stochastic synthetics, Part 2: Rupture parameters and variability. *Bulletin of the Seismological Society of America*, *108*(5A), 2370-2388.

Yin, Y., Wang, F., & Sun, P. (2009). Landslide hazards triggered by the 2008 Wenchuan earthquake, Sichuan, China. *Landslides*, *6*(2), 139-152.

3.7 APPENDIX TO CHAPTER 3

Supplementary Text

3.7.1.1 Landslide Dating

Dates from 14 landslide deposits are used to regress the roughness-age function used to estimate all landslide ages in this study (Table S1). These dates come from this and other studies, and dating methods include radiocarbon, repeat aerial photography, dendrochronology, and, in one case, sediment aggradation rates in landslide dammed lakes (landslide ID#7). Radiocarbon dates of woody debris trapped within excavated landslide deposits are assumed to record the timing of trees killed by the landslide, and therefore offer a maximum age close to the timing of landslide failure. Radiocarbon dates from charcoal are used to constrain the age of one landslide, the Sitkum Landslide, but because charcoal has been shown to potentially persist in landscapes for many hundreds to thousands of years (Gavin, 2001; Gavin, Brubaker, & Lertzman, 2003; Struble et al., *in press*), this age is taken to represent a maximum age of failure. Previous age estimates for the Sitkum Landslide derived from upstream aggradation rates due to landslide damming were used as an approximate minimum age (Lane, 1987), and this data point was prescribed a relatively large uncertainty due to these methods. Dendrochronology offers the most accurate method of landslide dating, but is confined to landslides which preserve large, intact portions of tree trunks either within the deposits themselves, or as drowned stumps in dammed lakes adjacent to the deposit. We used dendrochronology dates from Struble et al. (*in press*) for 3 landslides (Table S1). To locate the most recent failures in the dated landslide inventory, we reviewed historical records from the Oregon Department of Geology and Mineral Industries (Burns, 2017) and used historical imagery from the last 25 years available on Google Earth.

3.7.1.2 Roughness Calculation

There are many ways to measure the surface roughness from a digital elevation model (DEM). The goal of roughness dating is to find a method which best tracks landslide age, so that roughness alone can be used as an age proxy. We tested 3 different roughness metrics that proved most accurate for tracking landslide age in glacial sediments (Booth et al., 2017): mean standard deviation of slope in a 15m window, spectral power sum from 10m-30m wavelengths using a Fourier transform, and mean wavelet-based curvature using a Mexican hat continuous wavelet transform (CWT) at multiple length scales. Values for each metric were computed from within mapped landslide deposit polygons and plotted against independent landslide age constraints from radiocarbon, dendrochronology, or repeat aerial imagery. We use standard error (SE) as a measure of fit accuracy and compare SE for the entire dataset as well as SE specifically for the last 1,000 years, as minimizing the error for these youngest ages is important for interpreting trends in the landslide frequency data we eventually generate.

Results show that the Mexican Hat CWT at a 20m scale produces the smallest SE for the last 1 kya: ~200 yrs (Table S2). Every other technique resulted in SE at least double this value. The SE for the entire dataset is minimized using the spectral power sum of 10-30m wavelengths from the Fourier Transform, but it is only marginally smaller than the SE using the 20m Mexican hat: 1500 yrs versus 1600 yrs, respectively (Table S2). Because of the overall performance of the 20m Mexican Hat CWT, we chose this technique as our roughness metric for this study.

3.7.1.3 Landslide Mapping and Roughness Error Estimation

We assume that error in measured mean roughness values for landslide deposits stems from two primary sources: errors in manually mapped landslide polygons and variations in lidar quality. Manually delineating individual landslide polygons and classifying them as single events is inherently subjective in nature, so we conducted all mapping based on the following objective criteria to minimize this bias:

1. Landslides must have an arcuate or scalloped headscarp which bounds, but is not included within, the upper portion of the slide deposit polygon.
2. Only slides that we deem 'coherent' are mapped. We interpret coherent slides to be deep-seated, which we define as having a headscarp >2m tall and failing within bedrock or older landslide deposit and not within colluvium or regolith alone. Furthermore, coherent slide deposits must display hummocks, extensional fractures, compressional ridges, or rigid blocks. We exclude landslides with channelized flowpaths or elongate ridges in the direction of flow, which both indicate a high degree of fluidization and/or disintegration of the landslide body during failure. These more fluid landslide styles, including rock avalanches, debris flows, and earthflows, do not consistently form the types of deposits with high initial roughness, and are therefore not suitable for roughness dating.
3. All erosional contacts, including river cutbanks and younger landslide scarps are excluded from mapped polygons before analysis. We prioritize exclusion of non-landslide landforms over completeness of landslide deposit extent when mapping. Stream gullies on the surface of landslide deposits are excluded wherever they are observed.
4. Man-made structures, including roads, are removed along with a buffer around these objects. Road data was provided by the Oregon Spatial Data Library run by the State of Oregon.

5. All landslides interpreted as complexes are mapped as separate component landslides, based on the presence of internal scarps and the visual appearance of multiple generations of failure, including a difference in visual roughness, the sharpness of headscarps, and the degree of stream gully development.

While the uncertainty in how accurately landslides are mapped is difficult to quantify, we assume that it is less than the uncertainty due to varying lidar quality. Variations in ground point density used to produce the DEMs provided by the Oregon Department of Geology and Mineral Industries (DOGAMI) result in measurable differences (Burns et al., 2010), including in our calculated roughness. Most lidar surveys in the Oregon Coast Range, regardless of point density, have been converted to DEM raster files at a 3 foot (0.91m) resolution and distributed by DOGAMI where it was downloaded for this study (a small portion of the Umpqua River watershed was gridded at 1m, but was resampled at 0.91m to ensure the same cell size across the study area before roughness analysis – none of the landslides used in the roughness-age regression were mapped in that particular region). Because point density used to create DEMs varied, some portions of the study area have highly accurate ground surface data, while others appear as a mesh of triangulated facets – the result of ground point spacing greater than the cell size. These lower resolution portions may artificially smooth small, sharp hummocks, making rough surfaces appear smoother, and may introduce artificial facets to otherwise smooth surfaces.

Unfortunately, there are not multiple lidar datasets for much of the study area, otherwise we would have directly measured the difference in calculated roughness values between datasets for individual landslides used in the roughness analysis. Instead, we took advantage of a repeat lidar survey in the Panther Creek region of the Oregon Coast Range, with datasets from 2011 and 2015. We divide the overlapping portions of the dataset into 272 cells at a 250m grid spacing, so that each cell had an area equal to the average area of all mapped landslides in the study: ~60,000 m^2. We then calculate the mean roughness using the 20m Mexican hat CWT in each grid cell for both datasets and then take the absolute value of the difference. This resulted in a mean roughness coefficient difference of $1.05*10^{-3}$, a median of $6.58*10^{-4}$, and a maximum of $1.05*10^{-2}$ (2.7%, 1.4%, and 61.9%, respectively). We plot the distribution of difference values and calculate a 2σ range of $6.30*10^{-3}$ ($\pm 3.15*10^{-3}$), which we apply as error bars in Figure 3. In the future, we would expect new lidar data with better ground point coverage to reduce SE between the regression and the data and thereby improve age estimations.

3.7.1.4 Effect of Natural Variability in Roughness on Simulated Landslide Frequency

For roughness-dating to operate with no error, all landslides of the same age would have identical roughness values. However, natural variability in the initial mean roughness of landslides (immediately after failure) represents a source of uncertainty separate from actual error in roughness measurements, as discussed above. This source of natural variability is likely driven by slightly different failure mechanics, geometries, and underlying structural and lithological variation. Fortunately, this natural distribution of mean roughness values should shrink rapidly over time, as the rougher landslides smooth at a much faster rate than the landslides of low initial roughness. This effect is supported by the exponential form of the roughness-age relationship.

The distribution of roughness values for landslides of a specific age directly affects the shape of the resulting age distribution using the roughness dating technique. Therefore, it is important to quantify the roughness variability as well as possible. For our 1,000-year simulated landslide histories, we chose a value for SD of roughness for which to distribute roughness values for earthquake pulses and for the background rate at each timestep in the model. The SD we chose needed to be both conservative and representative of our observed data. Because 4 landslides in our dataset of known landslide ages are within 100 years of the last great earthquake, in 1700 CE, we calculate the SD of these 4 points. We then double this measured SD for a more conservative measure, given the small sample size. A sensitivity analysis shows that the shape of landslide frequency versus time plots, which are estimated from the raw roughness values using the roughness-age regression, is highly dependent on the SD of roughness values used to generate landslides in the modeled simulations (Figure S2).

If sufficiently high SD values are used in the simulations, all ages are heavily skewed towards zero: a product of passing a normal distribution through an exponential predictor function. However, SD values of up to double that used in the simulations in this paper (and therefore 4 times the measured SD) still produce rapid decays in frequency towards present day. Moreover, a SD value high enough to erase this rapid drop in frequency towards present day by skewing frequency values towards zero would likely result in an empirical dataset of landslides of known ages that is not well fit by an exponential function. At the very least, if such high SD of roughness values existed in the study area, dated landslides would tend to produce much greater standard errors, and lower R^2 values, when fit with any regression. Collectively, this suggests the SD we adopt for our modeled landslide simulations is reasonable, and supports the conclusions drawn from analysis of these simulations.

Supplementary Figures and Tables

Table 3.3. Landslides with independent age constraints used to regress the roughness-age function. Landslide size, location, and average roughness (mean wavelet coefficient magnitude). Dating methods, ages and uncertainties, and sources are listed, as well as the age value used in this study for the roughness-age regression (Figure 3.3)

ID #	**Name**	**Area (m^2)**	**Lat/ Long**	**Mean CWT coefficient magnitude (roughness, m^{-1})**	**Dating Method**	**Dates (years before 2019)**	**Age used in regression**	**Source**
1	LittleMill_ 009	$1.1*10^4$	43.700; -123.795	$12.42*10^{-2}$	Repeat Aerial Imagery	7±1	7	Burns (2017), this study
2	NA	$3.0*10^4$	44.195; -123.84	$6.479*10^{-2}$	Repeat Aerial Imagery	15	15	This study
3	Cummins_ Peak_475	$2.0*10^4$	44.135; -123.982	$7.423*10^{-2}$	Repeat Aerial Imagery	15	15	Burns (2017)
4	NA	$7.1*10^4$	44.373; -123.519	$6.720*10^{-2}$	14C from drowned stump	249±100	249±100	This study
5	NA	$7.9*10^4$	44.237; -123.429	$6.954*10^{-2}$	[1]14C from drowned stump [2]Post-slide tree stump ring count	[1]249±44 455±82 [2]>330+?	350±200	This study
6	Holt Log Reservoir	$2.5*10^5$	44.241; -123.501	$6.947*10^{-2}$	14C from log buried in deposit	295±56	295±56	This study
7	Sitkum	$2.2*10^6$	43.138; -123.89	$5.064*10^{-2}$	[1]14C from charcoal in deposit [2]Sedimentation rates of alluvial backfill	[1]4,110±82 [2]3,125 ±?	3,000 ±1,100	[1]This study [2]Lane (1988)
8	Drift Creek	$1.3*10^5$	44.461; -123.788	$6.408*10^{-2}$	Historical Observation	44	44	Burns (2017)
9	Loon Lake	$4.2*10^5$	43.599; -123.851	$5.362*10^{-2}$	[1]14C from drowned stump [2]14C from leaf in lake core	[1]1,460±80 [2]1,505±100	1,500±120	[1]Baldwin (1958) [2]Richardson (2018)
10	Little Lobster	$1.3*10^5$	44.311; -123.648	$7.371*10^{-2}$	[1]14C from buried log [2]Dendrochronology from buried log	[1]239±30 [2]<268	268	[1]This study [2]Struble et al. (2019)
11	Triangle Lake	$5.1*10^5$	44.162; -123.581	$2.927*10^{-2}$	Extrapolation of lake core record from 14C dates	41,800	41,800±1000	Worona & Whitlock (1995)
12	Burchard Lake	$9.2*10^4$	43.666; -123.769	$6.734*10^{-2}$	Dendrochronology from drowned stump	129	129	Struble et al. (2019)
13	Esmond Lake	$2.7*10^5$	43.878; -123.599	$6.577*10^{-2}$	Dendrochronology from drowned stump	129	129	Struble et al. (2019)
14	Eddy Creek	$4.2*10^5$	44.628; -123.793	$2.824*10^{-2}$	14C from buried log	40,900±570	40,900±1,000	Hammond et al. (2013)

Table 3.4. Standard error between roughness-age regression and landslides of known age for 5 different roughness metrics. SE for entire dataset and for a subset of the last 1 kya shown.

Roughness metric	Standard error (yrs)	Standard error for last 1 kya (yrs)
Mexican hat wavelet (4m)	5600	600
Mexican hat wavelet (15m)	2100	400
Mexican hat wavelet (20m)	1600	200
Spectral power sum (10-30m)	1500	600
Standard deviation of slope (15m window)	5000	400

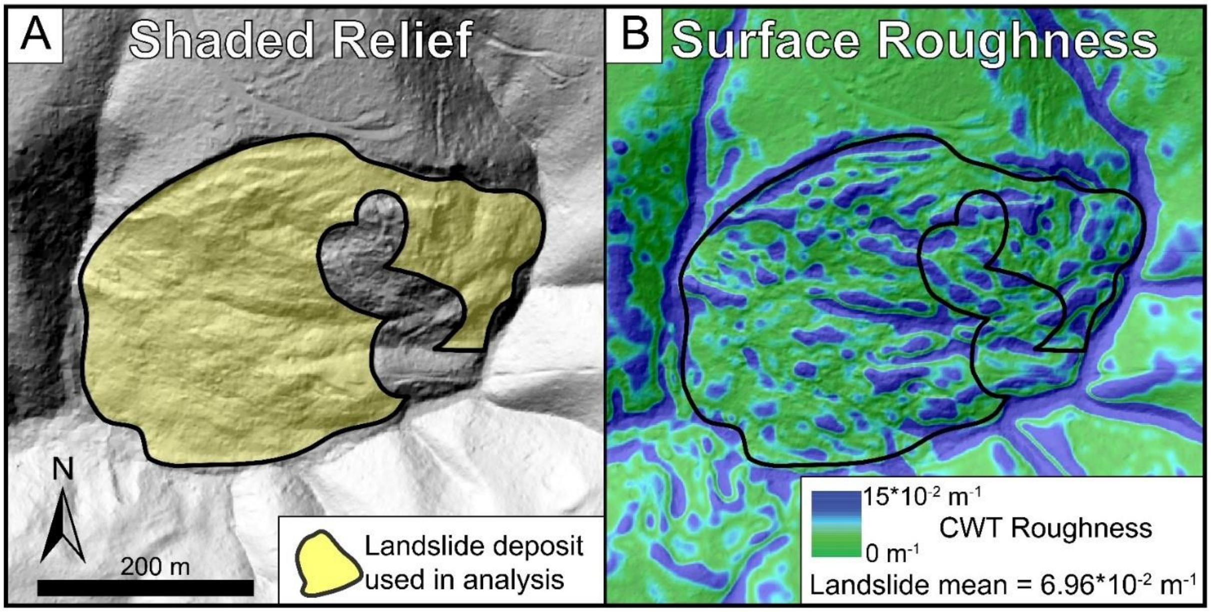

Figure 3.6. Landslide deposit polygon and results from surface roughness analysis for Landslide ID#5 (A) Hillshade map of landslide deposit #5 produced from 0.9m lidar bare-earth imagery. Polygon depicted in black shows region used in roughness-age regression. Note a buffer around a logging road has been removed from the polygon before analysis. (**B)** Surface roughness values across the landslide deposit, as measured by the absolute value of the continuous wavelet transform coefficient. Blue pixels represent areas interpreted as high roughness.

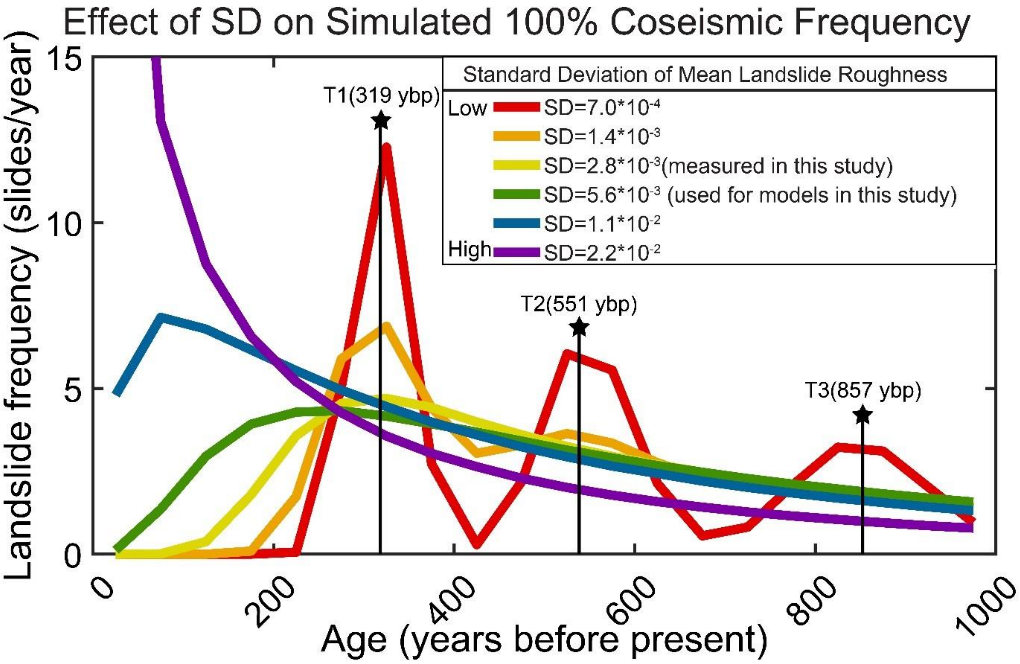

Figure 3.7. The effect of roughness variability on simulated landslide frequency. With all else held constant in simulated landslide histories, we show how the standard deviation of mean roughness for landslide pulses of the same age influences calculated landslide frequency. To best demonstrate the sensitivity of calculated frequency to SD, we use simulations where 100% of landslides are triggered by earthquakes (Figure 3.5C). We plot the mean of 10^3 model runs for each of 6 SD values. The same number of landslides (n=1,300) are prescribed in all simulations for each large CSZ in the last 5,000 years (only the last 1,000 years is plotted), so that only the effect of changing SD is shown. This analysis reveals that the SD value we use for simulations in this manuscript is too large to show discrete frequency peaks related to earthquakes but is sufficient to capture the dramatic drop in frequency towards present day that should be expected given the lack of large earthquakes since 1700 CE.

Supplementary References

Burns, W. J., Coe, J. A., Kaya, B. S., & Ma, L. (2010). Analysis of elevation changes detected from multi-temporal LiDAR surveys in forested landslide terrain in western Oregon. *Environmental & Engineering Geoscience*, *16*(4), 315-341.

Burns, W.J., 2017, Statewide Landslide Information Database for Oregon, release 3.4: Oregon Department of Geology and Mineral Industries, Web: http://www.oregongeology.org/sub/slido/

Gavin, D. G. (2001). Estimation of inbuilt age in radiocarbon ages of soil charcoal for fire history studies. *Radiocarbon*, *43*(1), 27-44.

Gavin, D. G., Brubaker, L. B., & Lertzman, K. P. (2003). Holocene fire history of a coastal temperate rain forest based on soil charcoal radiocarbon dates. *Ecology*, *84*(1), 186-201.

Chapter 4. REDUCED LANDSLIDE FREQUENCY IN RESPONSE TO REGIONAL HOLOCENE CLIMATE CHANGE

Deep-seated landslides are often triggered by precipitation, making them sensitive indicators of regional climate change. Here we show that a comprehensive landslide chronology in the Oregon Coast Range, USA reveals spatiotemporal shifts in landslide frequency through the Holocene that mirror independent paleoclimate proxies. We find a decrease in landslide frequency for locations in the present-day rain shadow relative to wetter present-day locations beginning in the early Holocene, a period that pollen and charcoal records suggest was warm and dry. A second, more dramatic reduction in landslide frequency occurs ~3,000 years ago, when the pollen record indicates a shift to a direr climate. We postulate that periods of drying in the early and late Holocene caused mean annual precipitation on the drier east side of the Oregon Coast Range to drop below levels required to trigger deep-seated landslides. On the wetter west side of the range, mean annual precipitation seems to have remained sufficiently high to maintain high landslide frequency, which may suggest a rainfall threshold for deep-seated landslide triggering in this region.

4.1 INTRODUCTION

Rainfall is the predominant trigger of non-coseismic landslides (Keefer, 1984; Caine et al., 1980; Petley, 2012). Because of the sensitivity of slope stability to precipitation, landslides can serve as a geomorphic record of local climate change through time (Gariano & Guzzetti, 2016). Establishing links between past landslide activity and paleoclimate also has important implications for validating predictive landslide hazard models, which are often influenced by the locations of past landslides (e.g. Lee, 2005; Ayalew & Yamagishi, 2005), and for assessing the effects of spatially heterogeneous future climate changes on landslide hazard (Jakob & Lambert, 2009). However, previous efforts to study the relationship between past climate changes and landslide frequency have been limited in their ability to construct comprehensive landslide chronologies, often focusing on a single site or even an individual slope failure (Gariano & Guzzetti, 2016). While ongoing lidar-based mapping efforts are constantly improving landslide inventories, establishing age constraints on the timing of landslide failures remains a challenge that prohibits our full understanding of spatiotemporal patterns in landslide processes. Here we use a comprehensive landslide chronology of 9,938 deep-seated landslides across 10,000 km^2 in the Tyee Formation of the central Oregon Coast Range – OCR (Chapter 3) to explore how spatial patterns in landsliding have changed from the late Pleistocene to the present day and interpret these changes with respect to the local paleoclimate record and modern mean annual precipitation (MAP). This investigation represents the largest spatial coverage of any paleo-landslide analysis to date.

4.2 BACKGROUND

Mapped Landslide Chronology

We examined spatial and temporal patterns in the landslide chronology mapped by LaHusen et al. (Ch. 3; Figure 4.9). This inventory includes 9,938 deep-seated, coherent landslides in the Tyee and overlying Elkton Formations of the OCR. As described in Chapter 3, we define coherent landslides as slope failures where the mobilized material has not completely disintegrated to the point of allowing flow or avalanche style runout. Landslide deposits were manually mapped using 0.9-1m bare-earth lidar imagery, based on the presence of an arcuate headscarp above and directly adjacent to hummocky or benched topography. Shallow landslides and flow-style slides were excluded from the inventory, as they are less suitable for surface roughness dating. Each landslide in the chronology has an estimated age from the roughness-age regression calibrated in LaHusen et al. (Chapter 3). Landslides estimated to be less than 1,000 years have a 2σ error of ±~1,000 years, while landslides thousands of years old have uncertainties of a few thousand years (LaHusen et al., Chapter 3). Due to this large uncertainty, we cannot identify the age of an individual slope failure precisely, but we can interpret statistically robust spatial patterns between subsets of landslides with substantially different age ranges, especially when applied to large inventories of mapped landslides.

Landslide Triggering

In addition to the nearly ~10,000 landslides we consider in this study, thousands more landslides have been mapped in coastal Oregon and Washington States outside our study area (Burns, 2012; Burns et al., 2017; Mickelson & Slaughter., 2017). Though determining the triggering mechanism for landslides across Cascadia remains a challenge, recent work suggests that despite the proximity of the OCR to the Cascadia Subduction Zone megathrust fault, little evidence exists in the landscape for widespread coseismic landsliding. Rather, rainfall seems to be the predominant landslide triggering mechanism (LaHusen et al., Ch. 3; Struble et al., *in press*; Struble et al., 2019). The relationship between rainfall intensity and duration and landslide triggering has been well-documented on a global scale (e.g., Caine et al., 1980; Guzetti et al., 2008). Intense precipitation can cause rapid increases in pore water pressure in the uppermost 1-2 meters of soil and regolith, effectively reducing normal stress between particles on a potential basal slip surface and triggering shallow slope failures and debris flows (Lu & Godt, 2013). Deep-seated landslides, those with basal slip surfaces that extend to depths of at least 2 meters, are typically less sensitive to short-term rainfall intensity than shallow slides, but require more total rainfall to be triggered (Van Asch et al., 1999). Although this makes deep-seated landslide triggering more difficult to predict (Polemio & Sdao, 1999; Van Tien et al., 2018), the links between deep-seated slides and rainfall are robust (Iverson, 2000; Ayalew, 1999; Zêzere, et al., 2005). Increases in mean annual precipitation as little as 10%-20% have been linked to reactivation of dormant landslides in Switzerland (Lateltin et al., 1997). On longer timescales, landslide activity has been shown to track wetter time intervals in paleoclimatic reconstructions from the late Pleistocene to near present-day (Soldati et al., 2004; Bolgatti & Soldati, 2010).

Climate of the OCR from Pleistocene to present-day

The central OCR is currently characterized by mild temperatures year-round, but exhibits strong seasonality in precipitation, with wet winters and dry summers (Taylor & Barlett, 1993). MAP for the last 30 years ranges from 1,040 mm/yr to 4,070 mm/yr (PRISM Climate Group), though these lower and upper extremes effect very little area; 95% of the study area falls between MAP values of 1150 mm/yr and 2700 mm/yr (Figure 4.10). The OCR forms a topographic barrier to storms approaching from the west, resulting in a pronounced orographic effect that limits MAP on the east side of the range approximately half that of the west side (Smith et al., 2005; PRISM Climate Group). Our study area straddles this boundary, offering the ability to explore effects of this modern-day rain shadow on landslide frequency. Our landslide chronology extends from present day to at least 42,000 ybp (the oldest landslide used to calibrate the roughness dating curve). This study focuses on the last 30,000 years - a span of time which captures dramatic climate changes from the end of the Olympia nonglacial interval (59,000-25,000 ybp) to the last glacial maximum of the Cordilleran icesheet at ~16,400 ybp (Porter & Swanson, 1998) and through the entire Holocene (11,700-present day). Because no portions of our study area were glaciated, the effect of climate can be studied in a landscape not ‘reset’ by substantial glacial erosion. The best records of paleoclimate for the region come from numerous studies of lake cores collected from Little Lake, a landslide dammed lake in the east-central portion of our study area. Radiocarbon dates act as independent age constraints to interpret pollen (Worona & Whitlock, 1995), charcoal (Long et al., 1998), and ^{10}Be derived erosion (Marshall et al., 2017) records. Pollen records suggest a decrease in temperature from the end of the Olympia non-glacial into the Fraser glaciation ~25,000 ybp, followed by increasing temperature coming out of the glaciation beginning around 16,000-17,000 ybp. ^{10}Be concentrations show an uptick in erosion rates from the Olympia non-glacial to the Fraser glaciation interpreted to represent an increase in frost cracking due to a cooling temperature. Collectively, the paleoclimate record shows a cold and dry glacial period, with mean annual temperature estimated to be as much as seven degrees below present day, and MAP 50% of modern (Worona & Whitlock, 1995; Marshall et al., 2017). Though the Holocene was altogether warmer and wetter than the last glaciation, pollen and charcoal records suggest there were fluctuations in both temperature and precipitation during this time, with both records indicating a warm and dry early Holocene that lasted until ca. 6,000 ybp followed by a wetter middle Holocene (Long et al., 1998; Marshall et al., 1995). Enigmatically, the different climate proxies record contradictory evidence for the last 3,000 years. The pollen record shows a simultaneous increase in Douglas Fir abundance and decrease in Red Cedar and Red Alder, interpreted to be the result of climate drying around 2,800 ybp (Worona & Whitlock, 1995), while decreasing charcoal accumulation rates suggest a decrease in fire frequency between 2750 ybp and 1500 ybp, followed by an increase over the last 1,000 years (Long et al., 1998).

4.3 METHODS

Landslide Spatial Density and Temporal Frequency Calculation

To better understand spatial patterns in landsliding across the study area, we calculated the density of mapped landslides as the number of landslides/km^2. First, landslide polygons were converted to centroid points, then the spatial density of landslide points was calculated within a 5 km-radius circular moving window. To illuminate any spatial changes in landslide occurrence through time, we then calculated density maps for two distinct age ranges of landslides which we refer to as recent (<1,000 ybp) and pre-Holocene (>11,700). This effectively divides landslides into those that are hundreds of years old versus those that are tens of thousands of years old, allowing us to be confident in the temporal separation between these two subsets despite large uncertainties associated with the roughness dating approach. Like many geologic processes, younger landslides are more likely to be preserved in the record as old slides are reactivated or eroded, leading to a preservation bias that has been noted in previous work (LaHusen et al., 2016; Booth et al., 2017; LaHusen et al., Ch. 3). As old landslides are reactivated over geologic timescales, the old deposits are removed or reset to a higher roughness values. Because of this phenomenon, areas of high pre-Holocene landslide density reflect not only pre-Holocene landslide activity, but also a relative lack of post-Holocene landslide activity, as post-Holocene landslides would have effectively reset and erased the topographic signature of pre-Holocene slide deposits. To highlight any spatial shifts in landslide density, we compared density maps between these two age ranges by first normalizing each, then subtracting the pre-Holocene density from the recent density. Using these difference maps between recent and pre-Holocene landslide density, we selected two subsets of mapped landslides contained within regions of density difference greater than 0.5 and below -0.5, which correspond to anomalously high and low relative rates of recent landsliding, respectively. Importantly, we selected all landslides contained in these regions, not just recent or pre-Holocene landslides. We then used the estimated ages of these landslides to calculate mean landslide frequency per square kilometer over the past 30,000 years for each region.

Mean Annual Precipitation (MAP) and Landslides

To understand the relationship between the present-day climate and recent landsliding, we compare spatial patterns of mean annual precipitation (MAP) with recent landsliding. First, we examined MAP data from the last 30-years at an 800m resolution (PRISM Climate Group), and qualitatively evaluated any spatial correlation with relative recent landslide density. We then tested whether there is a direct correlation between mean annual rainfall (MAP) and recent landslide triggering by extracting MAP values from the centroid locations of all recent landslides (<1,000 ybp). We then binned these landslide precipitation values into 50 mm intervals and calculated the frequency of landslides for each precipitation interval. To account for the areal distribution of MAP values, we normalized landslide frequency by the total area of each 50 mm MAP interval within the study area. Intervals of extremely low or high relative MAP which account for a small proportion of the study area were removed to avoid error associated with very small areas and numbers of landslides (Figure 4.10). We focused our analysis on the middle 95% of MAP values: 1150mm/yr to 2450mm/yr. The resulting area-normalized landslide frequency allows us to better understand the relationship between MAP and landslide triggering frequency for the last 1,000 years.

4.4 RESULTS

Spatial Distribution of Landslides through Time

Landslide density ranges from 0 to 3.4 landslides/km^2 across the study area, with an average value of 0.95 landslides/km^2. Density maps reveal a highly heterogeneous spatial pattern in landslide occurrence across the study area, which includes a 100 km long NE-SE trending region that contains few if any deep-seated landslides, hereby referred to as the ‘highly stable zone’ and five ‘hotspots of instability’, which exhibit anomalously high landslide density (Figure 4.1). The density maps of recent and pre-Holocene landslides reveal hotspots that fit within the overall density map, but differ substantially from one another (Figure 4.2a, B). Because of preservation bias toward younger landslides (LaHusen et al., 2016; Booth et al., 2017; LaHusen et al., Ch.3), these two age ranges encompass a similar number of slides (2,203 pre-Holocene, 2,673 recent). When the recent and pre-Holocene landslides are plotted by longitude, the mean of recent landslides is shifted by 0.11 degrees of longitude west, equivalent to ~9km at the latitude of the study area, compared to the mean of the pre-Holocene landslides. The longitudinal distribution of pre-Holocene slides is heavy-tailed, thus, the distance between the two landslide subsets is more pronounced when we consider the peaks of the distributions rather than the means. Probability density functions generated for each landslide subset show the peak of the recent slide distribution is 0.2-0.3 degrees (~18-27km) west of the pre-Holocene subset (Figure 2C). This shift in the longitudinal distribution of recent landslides is due to a pronounced absence of recent landslides on the east side of the study area. Even within hotspots of high overall landslide density, there are very few recent landslides (hotspots 1 and 4, Figure 4.1).

Landslides and Rainfall

The zone of low recent landslide density aligns well with the present-day rain shadow on the east side of the study area (Figure 4.3a). This spatial correlation is further supported by differencing the pre-Holocene landslide density from the recent landslide density, which highlights the discrepancies between the two landslide age groups (Figure 4.3b). Importantly, because of the tendency to preserve young slides as old slides are reactivated or removed by erosion, areas of negative density difference are much more likely to represent a decrease in recent landslide frequency than a higher-than-average rate of pre-Holocene landslide activity. We find that the modern day 1550mm MAP contour closely follows the boundary between regions of low and high relative recent landslide density (Figure 4.3b). Moreover, analysis of MAP extracted from recent landslide locations suggests rainfall exerts strong controls on landslide frequency in the study area as regions with MAP values of 2,300mm/yr see three times the landslide frequency per area than regions with MAP values of 1,150mm/yr (Figure 4.4).

To understand how landslide frequency has changed in time across this boundary, we separately examine landslide ages for the last 30,000 years in these two regions by selecting all landslides contained within zones of anomalously high recent density (red pixels, difference > 0.5) and low recent density (blue pixels, difference < -0.5). We bin landslide ages into 1,000-year intervals and convert the number of slides per 1,000 years into landslide frequency in landslides/yr/km^2 (Figure 4.5). When this area-normalized frequency and corresponding kernel density estimation are plotted for the last 30,000 years, both high and low recent density regions reveal an overall non-linear increase in landslide frequency from 30,000 ybp to ~3,000 ybp. This trend has been observed in all previous roughness dating chronologies and is the result of a preservation bias towards younger landslides rather than a real increase in frequency (LaHusen et al., 2016; Booth et al., 2017; LaHusen et al., *in prep*). However, whereas the magnitude of landslide frequency is roughly the same between the two plots, ranging from 30,000 ybp - ~10,000ybp, landslide frequency in zones of low recent density falls short of frequency in zones of high recent density from ~10,000 ybp onward (Figure 4.5C). After 3,000 years, frequency decreases for zones of low recent density, while remaining high for zones of high density, resulting in the largest deviation between in frequency between low and high recent landslide density zones during this time. To ensure this signal of decreasing frequency is robust given the uncertainty involved in using roughness-dating, we performed a bootstrap analysis using 10^4 possible roughness-age regressions, each producing a unique landslide frequency dataset. The mean of these runs also show a frequency decrease around 3,000-4,000ybp, albeit less abrupt, corroborating the observed signal (Figure 4.11, Figure 4.12).

4.5 DISCUSSION

Decreasing total precipitation should be expected to affect deep-seated landslide processes over long timescales (Gariano & Guzzetti, 2016). In the central OCR, we see a westward shift in landslide density between pre-Holocene present-day landslides. This corresponds with a substantial reduction in landslide frequency in regions of low relative recent landslide density compared to regions of high relative recent landslide density, starting around the beginning of the Holocene. This may correspond to a well-documented warm early Holocene period that persisted locally until ~6,000 ybp (Worona & Whitlock, 1995; Long et al., 1998; Figure 4.5). The abrupt reduction in landslide frequency for sites of low relative recent landslide density beginning around 3,000 ybp may indicate another period of drying following a wet middle Holocene. While this interpretation is supported by the pollen record (Worona & Whitlock, 1995), the charcoal accumulation record suggests decreased fire frequency, usually associated with wetter climates (Long et al., 1998). Interestingly, landslide frequency on the east side apparently continues decreasing through the wet middle Holocene. Though we do not observe significantly increased landslide frequency corresponding to the wetter middle Holocene, this may be due to the nature of our technique, which, because of the preservation bias of younger slides, is inherently more effective at identifying reductions in landslide frequency than increases. The resolution of our dating technique may simply be too coarse at estimating mid-late Holocene ages to accurately detect this undulation. Another possible explanation for the decrease in landslide frequency after 3,000 years is a single widespread triggering event, or pulse of landslides, that occurred around this time or earlier. Previous work has shown that a pulse of simultaneous widespread landsliding should be expected to appear as a diffuse peak in the frequency plots derived from roughness-dating, due to uncertainty in the technique (LaHusen et al., Ch.3). Here, however, the frequency plot of low recent relative density zones represents a widespread portion of the east side of the study area. This would require some trigger that would have affected the entirety of the east side of the study area, but not the west side, which seems unlikely.

Though this study demonstrates a strong correlation between modern MAP and landslide frequency, the few places in the study area with MAP values greater than 2,700mm/yr (97.5th percentile of CDF) are not uniformly characterized by unusually high recent landslide density (Figure 4.2a, Figure 4.3a). This suggests landslide frequency does not scale indefinitely with precipitation and may suggest precipitation-induced deep-seated landsliding is a threshold process in this region, requiring a minimum volume of rainfall integrated over some time to achieve sufficiently high pore pressures at basal slip surfaces to trigger failure. Collectively, our interpretations point towards a decrease in landslide rates on the east side of the study area in the early Holocene and again beginning ~3,000 ybp, potentially caused by climatic drying. Even if this drying reduced MAP uniformly across the study area, rainfall on the wetter west side of the OCR may have still been sufficient to regularly surpass deep-seated landslide triggering thresholds, while this threshold may have rarely been surpassed on the drier east side. This reduction in landslide activity would have allowed older landslide deposits on the east side of the study area to persist in the landscape, while they were reactivated and effectively erased from the record on the west side. These results have important implications for future landslide hazard assessments. If landslide maps with no age constraints were used to train logistical regression models of landslide susceptibility, the result would substantially overestimate hazard for much of the east side of the study area. Recent landslides do not occur uniformly in areas of high overall landslide density, due to the pronounced westward shift since the Holocene. The locations of high recent landslide density, while within the regions of high overall density, are focused on specific areas that can only be identified because of landslide age constraints. These results show the danger in using past landslide locations with no age constraints to predict future landslide susceptibility, while highlighting the utility of surface roughness dating to estimate landslide age on a regional scale. This study also illuminates the sensitivity of deep-seated landsliding to regional climate and implies that future climate changes will continue to strongly influence where and how often landslides occur in Cascadia. The past is only key to the future if the climatic and tectonic drivers of landslides in the past resemble those of the future.

4.6 FIGURES AND TABLES

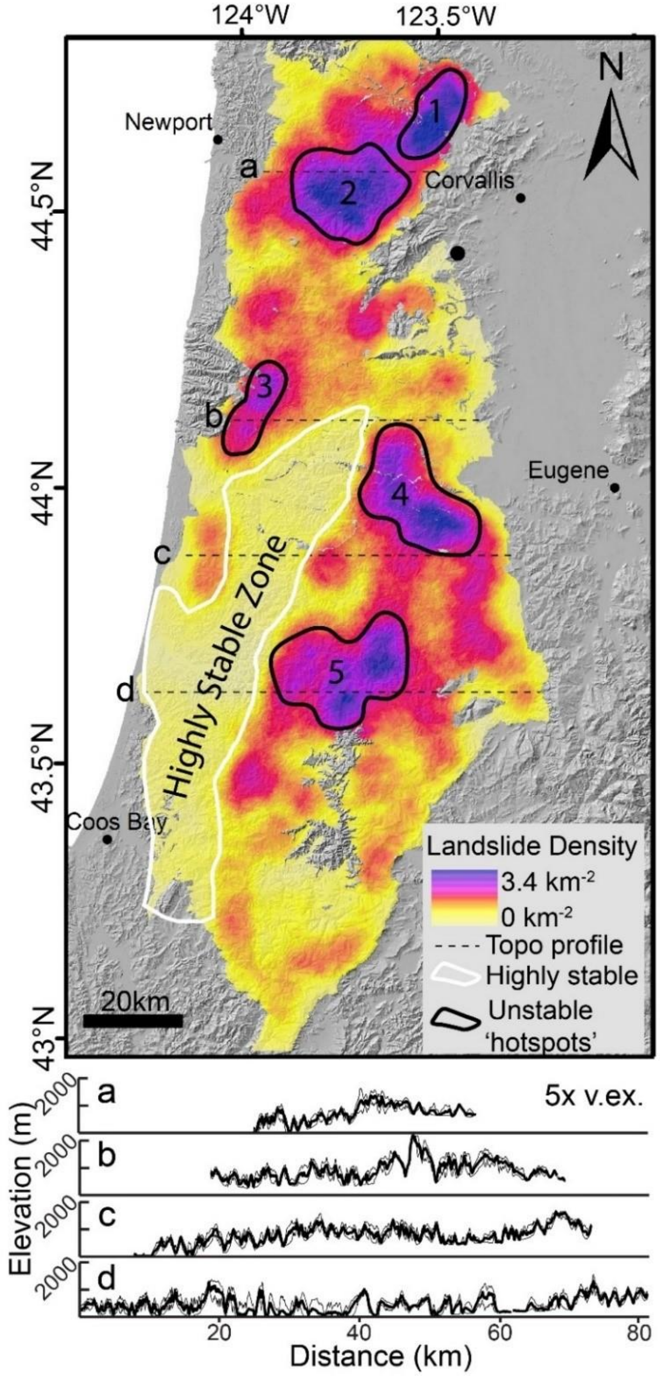

Figure 4.1. Landslide density across the study area, calculated in a circular moving window with 5km radius. Annotations show 100 km-long 'highly stable zone' characterized by anomalously low landslide density (0-0.5 slides/km^2) and five 'unstable hotspots' characterized by anomalously high landslide density (2-3.4 slides/km^2). Locations of four topographic swath profiles a-d shown as dashed lines. Topographic profiles below figure show max, min, and mean (bold) elevation in 2km band.

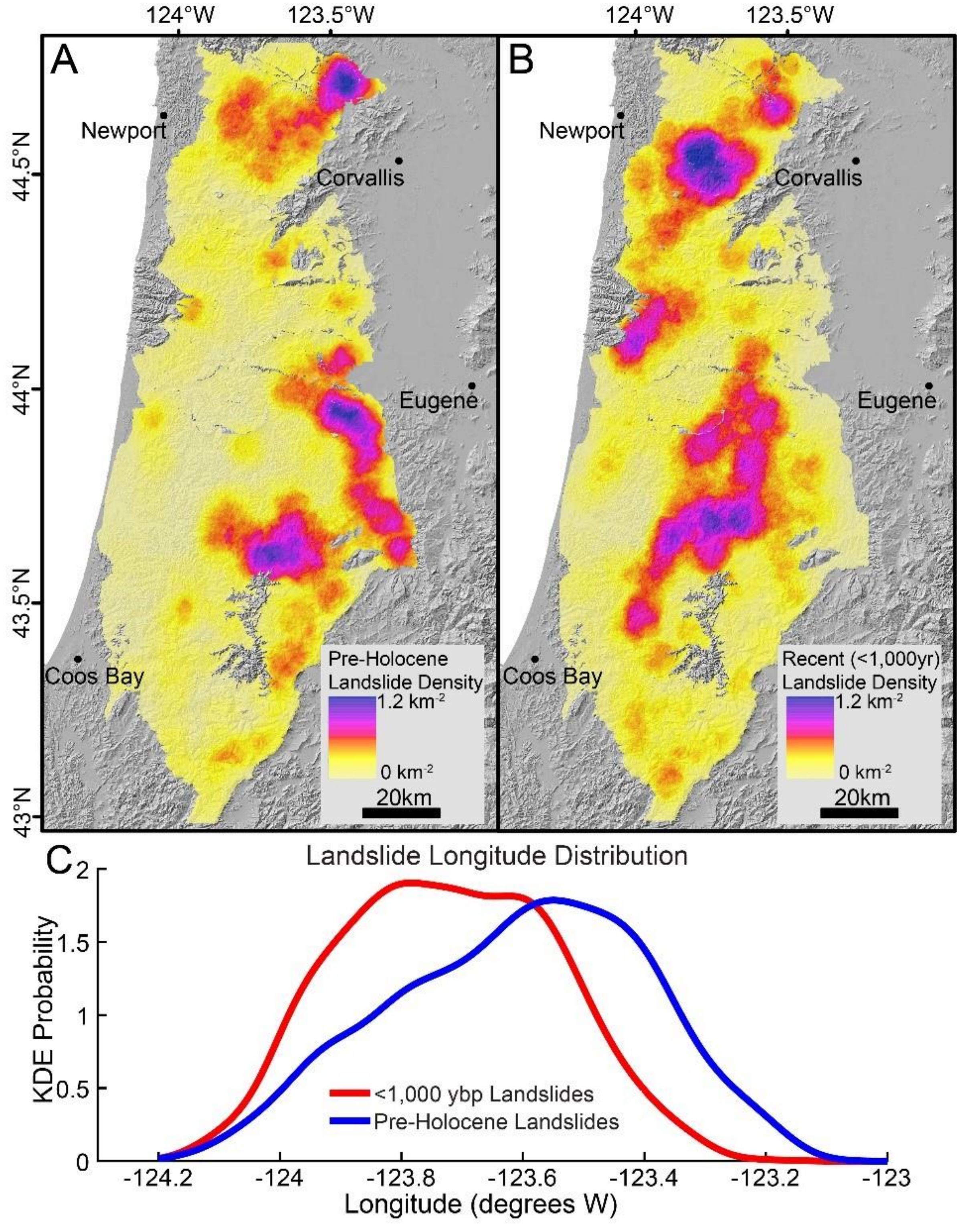

Figure 4.2. A. Spatial density of all landslides estimated to be older than Holocene (>11,700 ybp, n = 2,203). B. Spatial density of all recent landslides with estimated ages less than 1,000 ybp (n = 2,673). C. Kernel density estimation showing distribution of longitude for recent and pre-Holocene landslides, showing a relative westward shift in recent landslide.

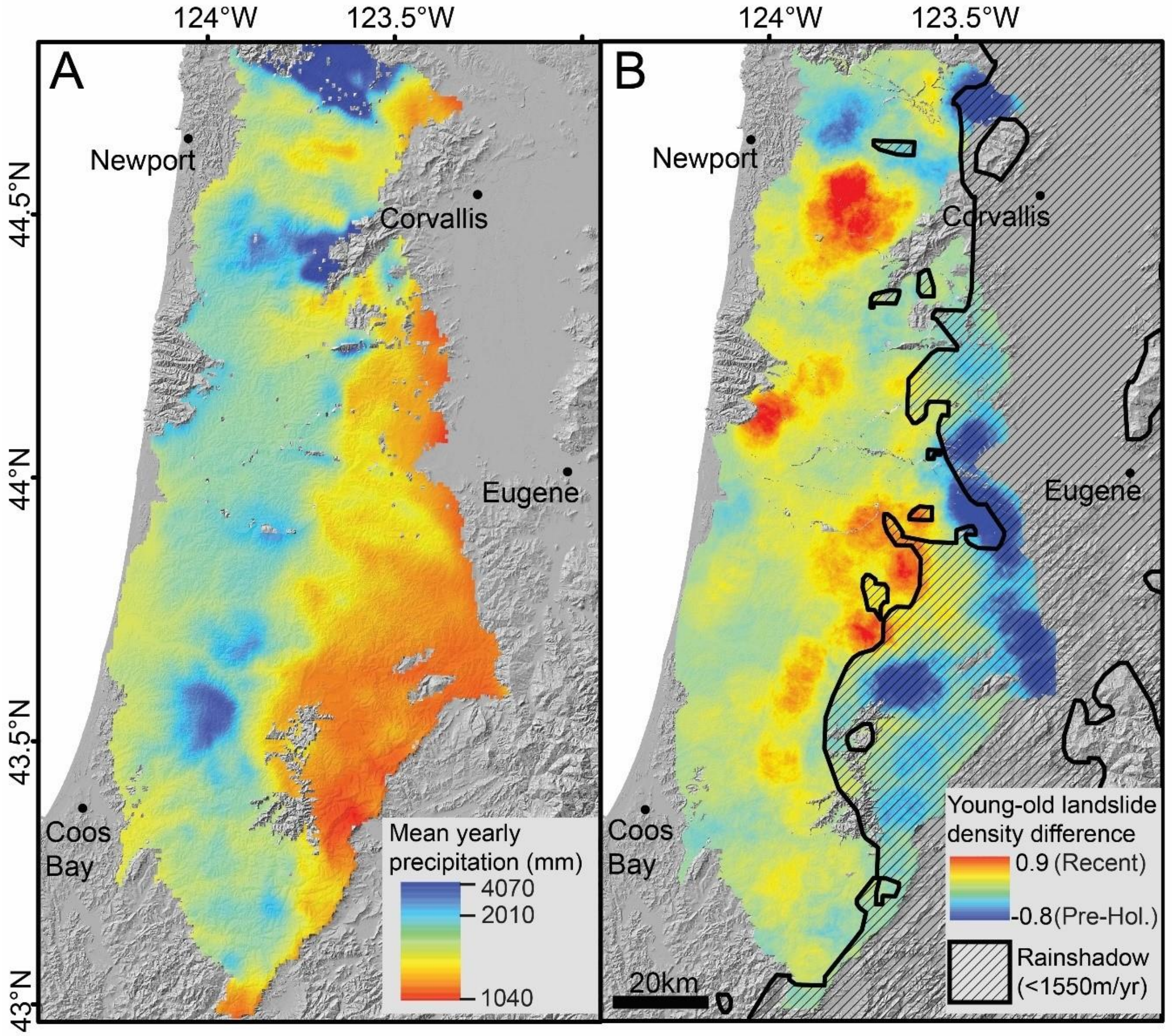

Figure 4.3. **A.** Mean annual rainfall for the last 30 years across the study area (source: PRISM Climate Group). **B.** Normalized pre-Holocene landslide density subtracted from normalized recent (<1,000 ybp) landslide density. Blue colors show regions with anomalously low recent landslide density. Hatched region shows areas which receive less than 1,550mm of rainfall/yr, highlighting the spatial correlation between the modern rain shadow across the Oregon Coast Range and the dearth of recent landslides on the east side of the study area.

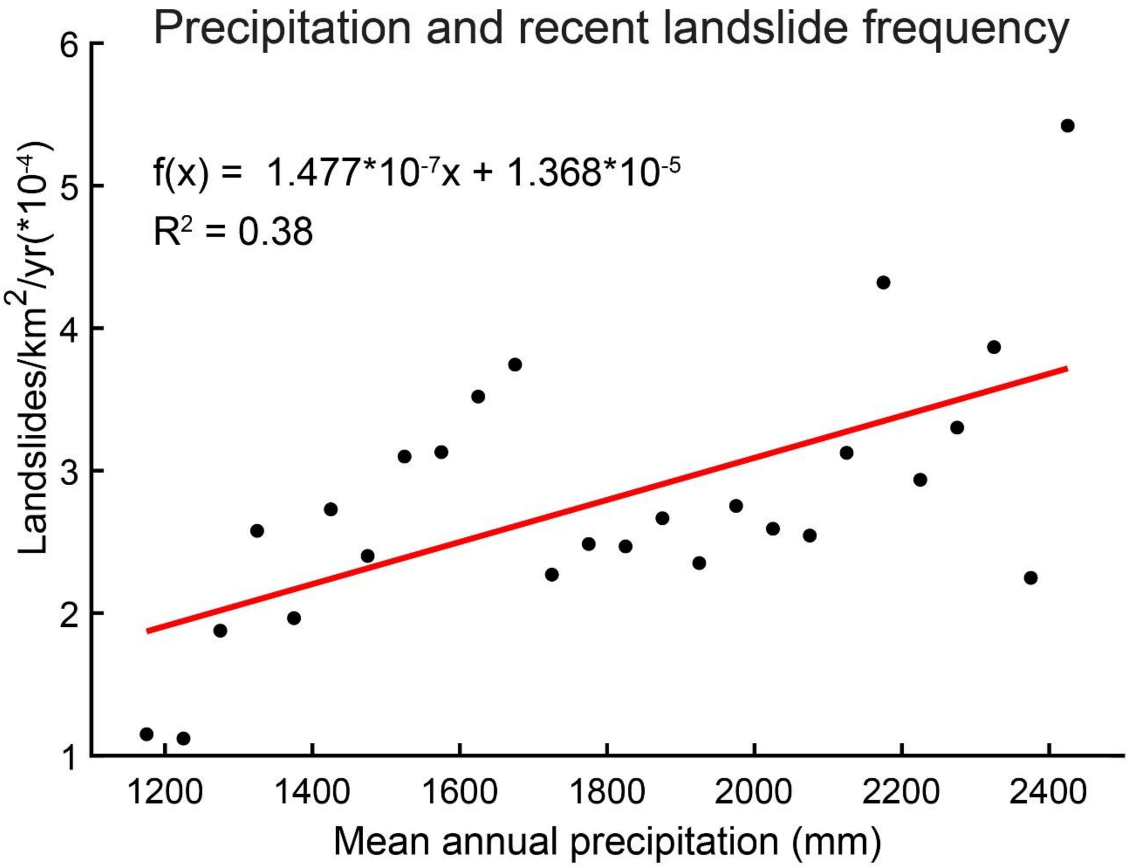

Figure 4.4. Plot of mean annual precipitation (MAP) versus landslide frequency in slides/km^2/yr for the last 1,000 years and best fit line. Landslide frequency was calculated by extracting MAP values (source: PRISM Climate Group) from the centroid of each recent landslide, binning these data into 50mm intervals, and dividing the total number of landslides for each precipitation interval by the total area each precipitation interval comprises within the entirety of the study area.

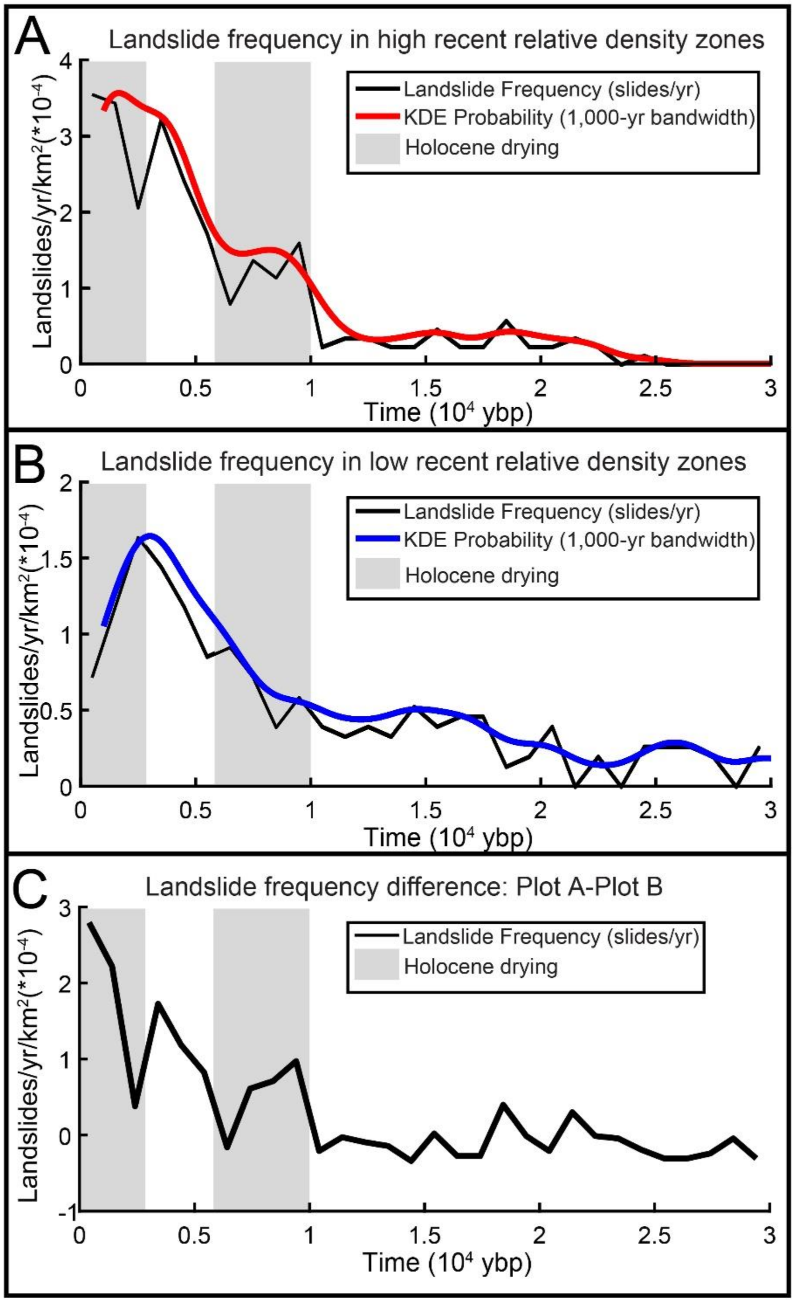

Figure 4.5. **A.** Landslide frequency per km^2 calculated at 1,000-year intervals for the last 30,000 years (black) and kernel density estimation (red) in regions of anomalously high recent landslide density, corresponding to all pixels in Figure 4.3b with values greater than 0.5 (n=226 landslides). Dry periods interpreted from the paleoclimate record shown in gray. Question mark indicates conflicting paleoclimate proxies: pollen record suggests drying while charcoal record suggests decreased fire frequency. **B.** Landslide frequency per km^2 (black) and kernel density estimation (blue) in regions of anomalously low recent landslide density, corresponding to all regions in Figure 4.3b with values less than -0.5 (n=295 landslides). **C.** Plot of the difference between landslide frequency in high relative recent density zones and landslide frequency in low relative recent density zones (plot A – plot B)

4.7 CHAPTER 4 REFERENCES

Ayalew, L. (1999). The effect of seasonal rainfall on landslides in the highlands of Ethiopia. Bulletin of Engineering Geology and the Environment, 58(1), 9-19.

Ayalew, L., & Yamagishi, H. (2005). The application of GIS-based logistic regression for landslide susceptibility mapping in the Kakuda-Yahiko Mountains, Central Japan. Geomorphology, 65(1-2), 15-31.

Booth, A. M., Roering, J. J., & Rempel, A. W. (2013). Topographic signatures and a general transport law for deep-seated landslides in a landscape evolution model. Journal of Geophysical Research: Earth Surface, 118(2), 603-624.

Booth, A. M., LaHusen, S. R., Duvall, A. R., & Montgomery, D. R. (2017). Holocene history of deep-seated landsliding in the North Fork Stillaguamish River valley from surface roughness analysis, radiocarbon dating, and numerical landscape evolution modeling. Journal of Geophysical Research: Earth Surface, 122(2), 456-472.

Borgatti, L., & Soldati, M. (2010). Landslides as a geomorphological proxy for climate change: a record from the Dolomites (northern Italy). Geomorphology, 120(1-2), 56-64.

Burns, B. J., Serin, D., Jones, C. B., & English, J. T. (2012) Open-File Report O-12-07, Lidar data and landslide inventory maps of the North Fork Siuslaw River and Big Elk Creek watersheds, Lane, Lincoln, and Benton Counties, Oregon

Burns, W.J. (2017). Statewide Landslide Information Database for Oregon, release 3.4: Oregon Department of Geology and Mineral Industries, Web: http://www.oregongeology. org/sub/slido/

Caine, N. (1980). The rainfall intensity-duration control of shallow landslides and debris flows. Geografiska annaler: series A, physical geography, 62(1-2), 23-27.

Densmore, Alexander L., et al. "Hillslope evolution by bedrock landslides." Science 275.5298 (1997): 369-372.

Densmore, A. L., & Hovius, N. (2000). Topographic fingerprints of bedrock landslides. Geology, 28(4), 371-374.

Gariano, S. L., & Guzzetti, F. (2016). Landslides in a changing climate. Earth-Science Reviews, 162, 227-252.

Guzzetti, F., Peruccacci, S., Rossi, M., & Stark, C. P. (2008). The rainfall intensity–duration control of shallow landslides and debris flows: an update. Landslides, 5(1), 3-17.

Iverson, R. M. (2000). Landslide triggering by rain infiltration. Water resources research, 36(7), 1897-1910.

Jakob, M., & Lambert, S. (2009). Climate change effects on landslides along the southwest coast of British Columbia. Geomorphology, 107(3-4), 275-284.

Keefer, D. K. (1984). Landslides caused by earthquakes. Geological Society of America Bulletin, 95(4), 406-421.

LaHusen, S. R., Duvall, A. R., Booth, A. M., & Montgomery, D. R. (2016). Surface roughness dating of long-runout landslides near Oso, Washington (USA), reveals persistent postglacial hillslope instability. Geology, 44(2), 111-114.

LaHusen, S. R., Duvall A. R., Booth A. M., Grant, A., Mishkin, B. A., Montgomery, D. R., Struble W., Roering, J. J., Wartman, J. (*in prep*). Rainfall triggers more deep-seated landslides than Cascadia earthquakes in the Oregon Coast Range, USA

Lateltin, O., Beer, C., Raetzo, H., Caron, C., 1997. Landslides in Flysch terranes of Switzerland: Causal factors and climate change. Eclogae Geol. Helv. 90, 401–406.

Lee, S. A. R. O. (2005). Application of logistic regression model and its validation for landslide susceptibility mapping using GIS and remote sensing data. *International Journal of Remote Sensing*, *26*(7), 1477-1491.

Long, C. J., Whitlock, C., Bartlein, P. J., & Millspaugh, S. H. (1998). A 9000-year fire history from the Oregon Coast Range, based on a high-resolution charcoal study. Canadian Journal of Forest Research, 28(5), 774-787.

Marshall, J. A., Roering, J. J., Gavin, D. G., & Granger, D. E. (2017). Late Quaternary climatic controls on erosion rates and geomorphic processes in western Oregon, USA. GSA Bulletin, 129(5-6), 715-731.

Mickelson, K. A., & Slaughter, S. L. (2017). Washington State's new landslide inventory mapping protocol. Washington State Department of Natural Resources, Washington Geological Survey. In GSA Annual Meeting, Seattle, Washington. October (Vol. 24, No. 2017, pp. 252-5).

Petley, D. (2012). Global patterns of loss of life from landslides. Geology, 40(10), 927-930.

Polemio, M., & Sdao, F. (1999). The role of rainfall in the landslide hazard: the case of the Avigliano urban area (Southern Apennines, Italy). Engineering Geology, 53(3-4), 297-309.

Porter, S. C., & Swanson, T. W. (1998). Radiocarbon age constraints on rates of advance and retreat of the Puget lobe of the Cordilleran ice sheet during the last glaciation. Quaternary Research, 50(3), 205-213.

PRISM Climate Group, Oregon State University, http://prism.oregonstate.edu, created 7 Oct 2019

Smith, R. B., Barstad, I., & Bonneau, L. (2005). Orographic precipitation and Oregon's climate transition. *Journal of the Atmospheric Sciences, 62*(1), 177-191.

Soldati, M., Corsini, A., & Pasuto, A. (2004). Landslides and climate change in the Italian Dolomites since the Late glacial. Catena, 55(2), 141-161.

Struble, W., Roering, J., Black, B., Burns, W., Calhoun, N., Wetherell, L. (*in revision*). Dendrochronological Dating of Landslides in Western Oregon: Searching for Signals of the Cascadia 1700 AD Earthquake. Geological Society of America Bulletin.

Struble, W., Roering, J., Black, B., Burns, W., Calhoun, N., Wetherell, L. (2019). Temporal clustering of landslide-dammed lakes in western Oregon using dendrochronology. Geological Society of America Abstracts with Programs 51(4), doi: 10.1130/abs/2019CD-329423

Taylor, G. H., and A. Barlett. (1993). The climate of Oregon, climate zone 1: Coastal Area. Oregon Climate Service, Oregon State University, Corvallis.

Van Asch, T. W., Buma, J., & Van Beek, L. P. H. (1999). A view on some hydrological triggering systems in landslides. Geomorphology, 30(1-2), 25-32.

Van Tien, P., Sassa, K., Takara, K., Fukuoka, H., Dang, K., Shibasaki, T., Ha, N.D., Setiawan, H. and Loi, D.H. (2018). Formation process of two massive dams following rainfall-induced deep-seated rapid landslide failures in the Kii Peninsula of Japan. Landslides, 15(9), pp.1761-1778.

Worona, M. A., & Whitlock, C. (1995). Late quaternary vegetation and climate history near Little Lake, central Coast Range, Oregon. Geological Society of America Bulletin, 107(7), 867-876.

Zêzere, J., Trigo, R. M., & Trigo, I. F. (2005). Shallow and deep landslides induced by rainfall in the Lisbon region (Portugal): assessment of relationships with the North Atlantic Oscillation. Natural Hazards and Earth System Sciences, 5(3), 331-344.

4.8 APPENDIX TO CHAPTER 4

Supplementary Figures and Tables

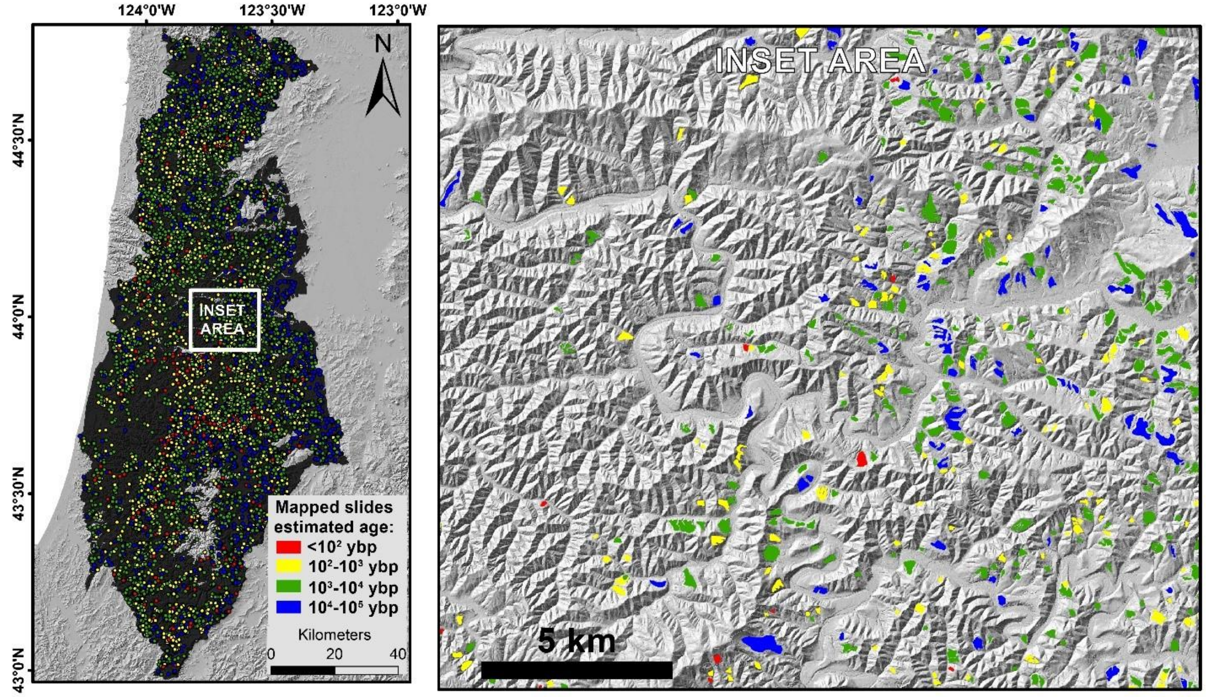

Figure 4.6. Map of all manually mapped landslides in the study area shown as points and colored by estimated age range. Mapping detail shown in inset area.

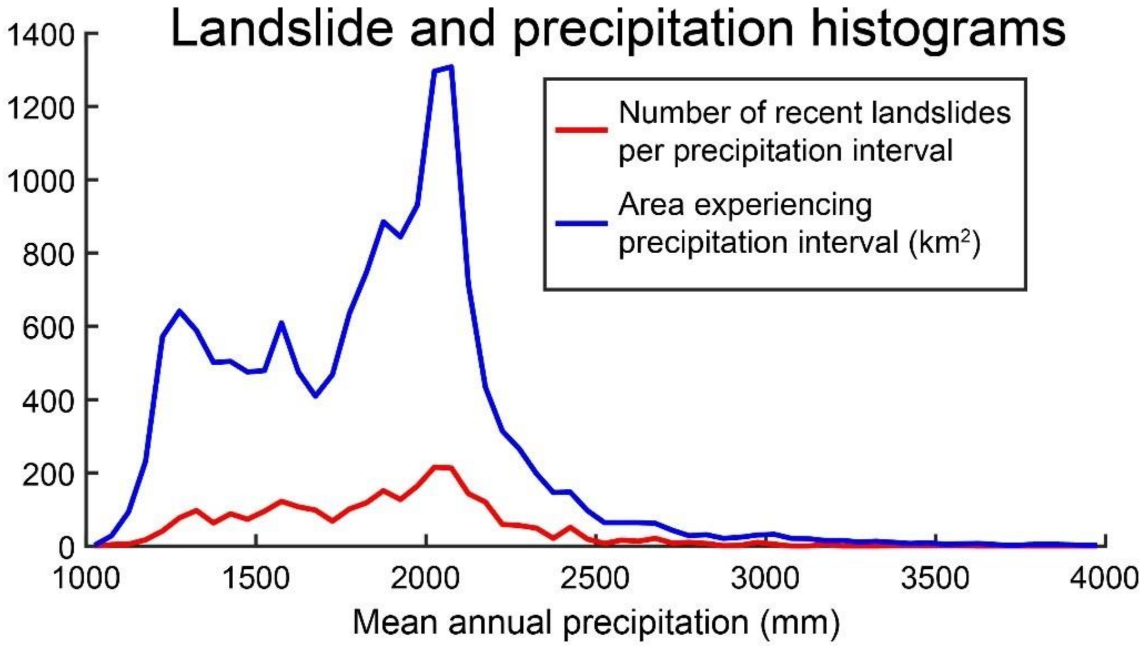

Figure 4.7. Histograms showing the areal distribution of mean annual precipitation (MAP) across the study area, binned into 50mm intervals (blue), and number of recent (<1,000 ybp) landslides located within each MAP interval (red). Figure 4 in the main text shows the quotient of these plots (#landslides/precipitation area) for each 50mm precipitation interval.

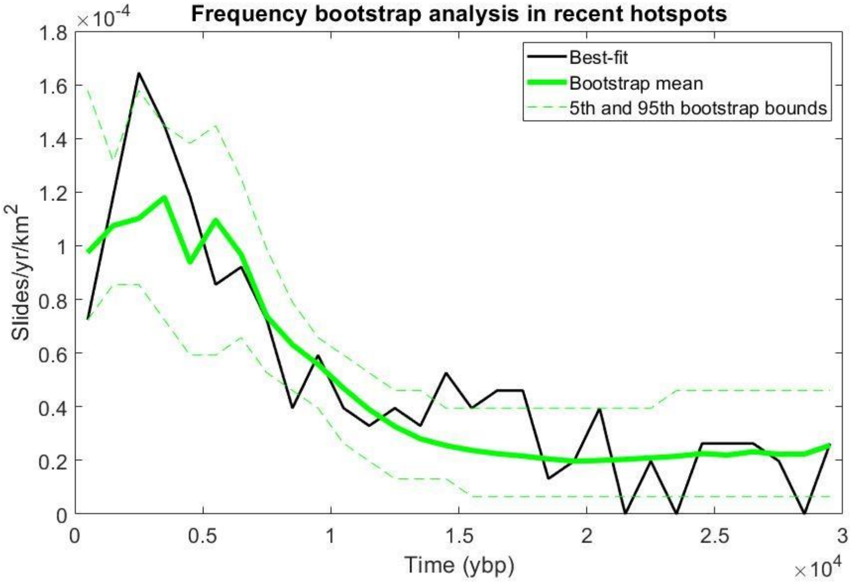

Figure 4.8. Mean yearly landslide frequency per km^2 calculated at 1,000-year intervals in regions of anomalously low recent landslide density (black), corresponding to all regions in Figure 4.3b with values less than -0.5 (n=295 landslides). A bootstrap analysis of 10^4 possible roughness-age regressions accounts for uncertainty in this frequency plot due to roughness-age regression parameters and is shown in green, where the solid line is the mean and the dashed lines are the lower 5th and upper 95th percentiles of the bootstrap analysis. Like the best-fit frequency plot in black, the bootstrap mean shows a decrease in recent in landslide frequency around 3,000 years ago.

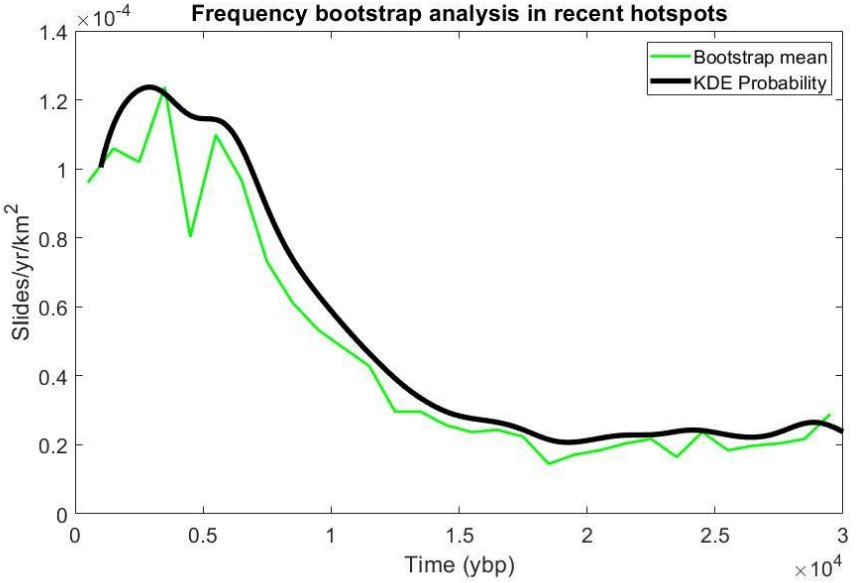

Figure 4.9. Yearly landslide frequency per km^2 in regions of anomalously low recent landslide density, corresponding to all regions in Figure 4.3b with values less than -0.5 (n=295 landslides). Kernel density estimation for all bootstrap runs shown in black and bootstrap mean frequency binned at 1,000-year intervals in green.

Chapter 5. CONCLUSIONS

Lidar has revealed thousands of previously unidentified landslides, underscoring the importance of this often-catastrophic process to shaping the surface of the earth on human and geologic timescales. The increasing availability of such high-resolution elevation data promises to rapidly improve our ability to map landslides and assess hazard and risk posed by unstable hillslopes. However, our ability to probabilistically assess landslide hazard and to quantify the geomorphic impact of landslides hinges on an understanding of when and how often they occur, which is difficult to measure. In this dissertation, I outline a new dating method for deep-seated landslides that can be applied on a regional scale wherever high-resolution elevation data exists. Surface roughness dating leverages independent age constraints from a subset of landslides to calculate a roughness-age function which can be used to date other mapped landslides in an inventory.

In Chapter 2, I test this method on a stretch of the North Fork Stillaguamish River valley immediately surrounding the devastating 2014 Oso Landslide in northwest Washington State. Results from this study show relatively high Holocene rates of landsliding in the region and suggest that landslides with similar destructive capacity to the 2014 event occur every few hundred years in the region. In Chapter 3, I manually map an inventory of nearly 10,000 deep-seated landslides in the central Oregon Coast Range. Using surface roughness dating, I examine trends in landslide frequency over the last thousand years to parse the importance of rainfall versus earthquakes as landside triggers. Despite the proximity of these landslides to the Cascadia Subduction Zone, where large earthquakes occur every few hundred years, I find little evidence for widespread coseismic landsliding, suggesting that precipitation triggers more deep-seated landslides in this region. This finding is corroborated in Chapter 4, where I show a correlation between mean annual precipitation and recently triggered landslides in this inventory. Moreover, I find periods of decreased Holocene landslide frequency within the rain shadow of the Oregon Coast Range. Some of these decreases align with dry periods in the paleoclimate record, revealing how a changing climate can impact the frequency of landslides in a spatially heterogenous manner.

Through this body of work, I show how using surface roughness as a proxy for landslide age can add the dimension of time to mapped landslide inventories, allowing for a more thorough exploration of landslide frequency, triggering mechanisms, and spatial changes in occurrence through time. Contributions from these studies have broad implications for our understanding of how landslides shape dynamic landscapes, and for improving landslide hazard assessments - a necessary step to quantify and mitigate risk.

APPENDIX A

This appendix contains results and interpretations from landslide susceptibility modeling of the Tyee Formation in the Oregon Coast Range. The study area is considered in this appendix is the same as in Chapters 3 and 4. Landslide susceptibility models are commonly used to predict relative landslide hazard or probability of occurrence across a region (Corominas et al., 2014). These models are generally based either on physical laws or logistical regressions (Guzetti et al., 2006). Results presented in this appendix are from physics-based models which rely on calculating the resisting versus driving forces acting on all potential failure locations across a landscape, with this ratio often referred to as the Factor of Safety (FS) (Lu & Godt, 2013). The parameters with the greatest influence on predicted susceptibility values are saturation, surface slope, peak ground shaking intensity from earthquakes, and material strength of the underlying bedrock or soil (Lu & Godt, 2013). While surface slope and sometimes peak ground acceleration can be accurately measured at high resolution across a region, material strength (cohesion and angle of internal friction) are often difficult to constrain and can vary over short distances. All landslides considered in this study are deep-seated, coherent landslides with basal slip surfaces assumed to be a few meters to hundreds of meters thick based on headscarp heights. Mechanically, these styles of landslides are often approximated by purely translational block slides (planar failure surfaces) and purely rotational (arcuate failure surfaces approximated by a circular projection into the hillslope) end member geometries, though in reality most landslides probably fail by some intermediate geometry between the two (Varnes, 1978). Recent multimodal landslide susceptibility modelling has shown the importance of accounting for different geometries that characterize these multiple failure styles (Grant et al., 2016; Pollock et al., 2019). Here we test two physics-based models, one for rotational landslides and one for translational landslides. Though we do not develop a logistical regression model, we discuss potential limitations of such a model by evaluating spatial changes in landslide frequency through time.

Because all mapped landslides are failing within minimally deformed Eocene marine sandstone and siltstones, we apply one set of rock strength parameters uniformly across the study area. We set cohesion equal to 1,000 kPa, and angle of internal friction equal to 30°, reasonable values for weak sandstone (Jafarpour, et al., 2012; Bandyopadhyay & Abdullah, 2013). We modeled both rotational and translational failure modes using two separate physics-based models (Grant et al., 2016). We first considered static factor of safety under saturated conditions. Factor of Safety (FS), which is the ratio between resisting and driving forces acting on a hypothetical failure mass, takes the general form:

$$FS = \text{resisting forces}/\text{driving forces}$$

For translational landslides, we adopted infinite slope criteria (Lu & Godt, 2013) which assumes infinite slope length and ignore forces acting on the sides of the sliding mass to simplify computation time. We calculated translational factor of safety for each 10 m pixel using the following equation:

$$FS = \frac{c + \left(\left((\rho_{rock}\mathrm{g}) - (m\rho_{water}\mathrm{g})\right)z\cos^2(\beta)\tan(\varphi)\right)}{\rho_{rock}\mathrm{g}z\sin(\beta)\cos(\beta)}$$

Here, c is cohesion in kPa, ρ_{rock} is the density of bedrock in kg/m^3, g is acceleration due to gravity, m is normalized water height above depth z, ρ_{water} is the density of water in kg/m^3, z is depth to failure plane, β is the angle of the slope at that location in radians, and φ is the angle of internal friction. For rotational landslides, we assumed a circular failure plane with radius 1.5

times the local landscape relief (Grant et al., 2016; Pollock et al., 2019). For this case, we calculated factor of safety using the using the following equation, after Pollock et al (2019):

$$FS = \frac{2\pi Rbc + (Wcos(\alpha) - F_w)\tan(\varphi))}{Wsin(\alpha)}$$

Here, c is cohesion in kPa and φ is the angle of internal friction. Parameters W (weight of the failure mass), F_w (force of pore water pressure), and α and b (geometric constraints) are calculated based on the radius of the circular failure surface (R), which depends on landscape relief (H) and surface slope (β), such that: $W = \frac{\pi\rho_{rock}gb^2}{3}(3R - b), F_w = \frac{\pi\rho_{water}gq^2(3R-q)}{3}$, and $\alpha = sin^{-1}(\frac{4(\sin\delta)^3 sin\theta}{3(2\delta - sin2\delta})$, where $b = R(1 - cos\delta), q = R(1 - cos\theta), R = \frac{H}{4}\left(\frac{cos\beta}{p(sin\beta)^2} + \frac{p}{cos\beta}\right), \delta = sin^{-1}\frac{H}{2Rsin\beta}$, p is a depth factor equal to 1.0, θ depends on the level of saturation, ρ_{rock} is the density of rock in kg/m^3, ρ_{water} is the density of water in km/m^3, and g is acceleration due to gravity. A simple relationship exists between FS and the theoretical ground acceleration required to make a slope unstable (Newmark, 1965), such that:

$$A_c = (FS-1)*sin(\beta)*g$$

Using this relationship, we then accounted for strong ground motions using modeled peak ground accelerations (PGA) from a suite of numerical simulations of CSZ magnitude 9 earthquakes (Frankel et al., 2018, Wirth et al., 2018). These simulations generate synthetic seismograms for dozens of earthquake scenarios, where model parameters that indirectly control ground motion generation have been systematically varied. In this study, we used the mean PGA values from all synthetic seismograms generated by Frankel et al. (2018) and Wirth et al. (2018), and then take the ratio of A_c:PGA, where lower values are interpreted to show locations with higher susceptibility for coseismic landslides. After modeling translational and rotational landslide susceptibility under static and dynamic conditions, we qualitatively evaluated model performance by comparing our landslide maps with maps of modeled landslide susceptibility.

Areas of low rotational landslide FS (high susceptibility) under static conditions do not align with mapped landslides (Figure A1). Translational landslide susceptibility is higher than rotational susceptibility on average, but still fails at identifying mapped landslides, or even zones of high landslide density (Figure A2). The magnitude of the average modeled FS of pixels within the mapped landslides is quite high: 2.6 for translational sliding and 3.7 for rotational sliding. While the magnitude of FS calculated by these susceptibility models is highly dependent on the rock strength parameters chosen for this study, adjusting these parameters would only change the overall magnitude of FS, which does not explain the lack of spatial correlation between modeled susceptibility and the mapped landslide locations. Accounting for strong ground motions from CSZ earthquakes increased susceptibility across the study area, but not uniformly. Because PGA from CSZ earthquakes is expected to decrease eastward, zones of high susceptibility were shifted westward – towards higher ground shaking, which did not improve accuracy for either rotational or translational slides (Figure A3).

This analysis suggests some spatially heterogeneous control on bedrock landsliding that is not accounted for in the landslide susceptibility models. I hypothesize that physics-based susceptibility models fail in the OCR because of variation in rock mass strength, due to some combination of lithologic and structural variability and reduction in shear strength due to previous slope failures.

Appendix A Figures

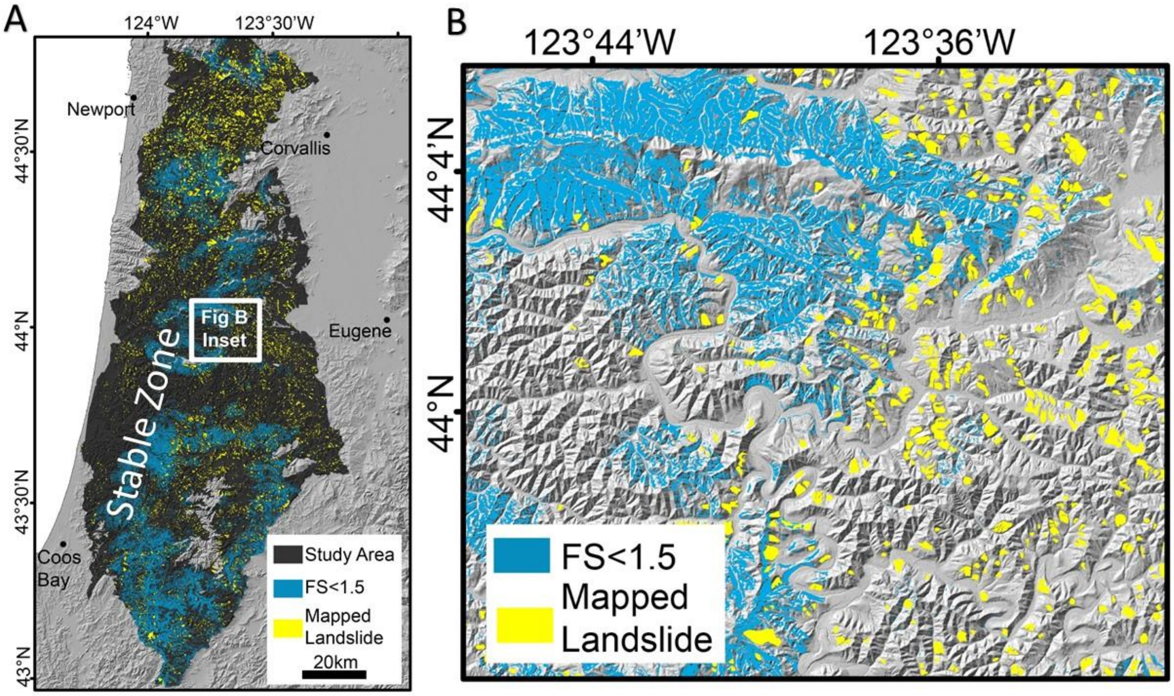

Figure A1. **A.** Modeled rotational landslide susceptibility under static, saturated conditions and mapped landslide deposits across the study area (shaded region). 10m pixels with modeled factor of safety less than 1.5 shown in blue, landslides mapped manually from 1m lidar shown in yellow. **B.** Detailed inset map shows poor landslide susceptibility model performance. The model consistently overpredicts susceptibility in areas without mapped landslides and underpredicts in areas with high densities of mapped landslides.

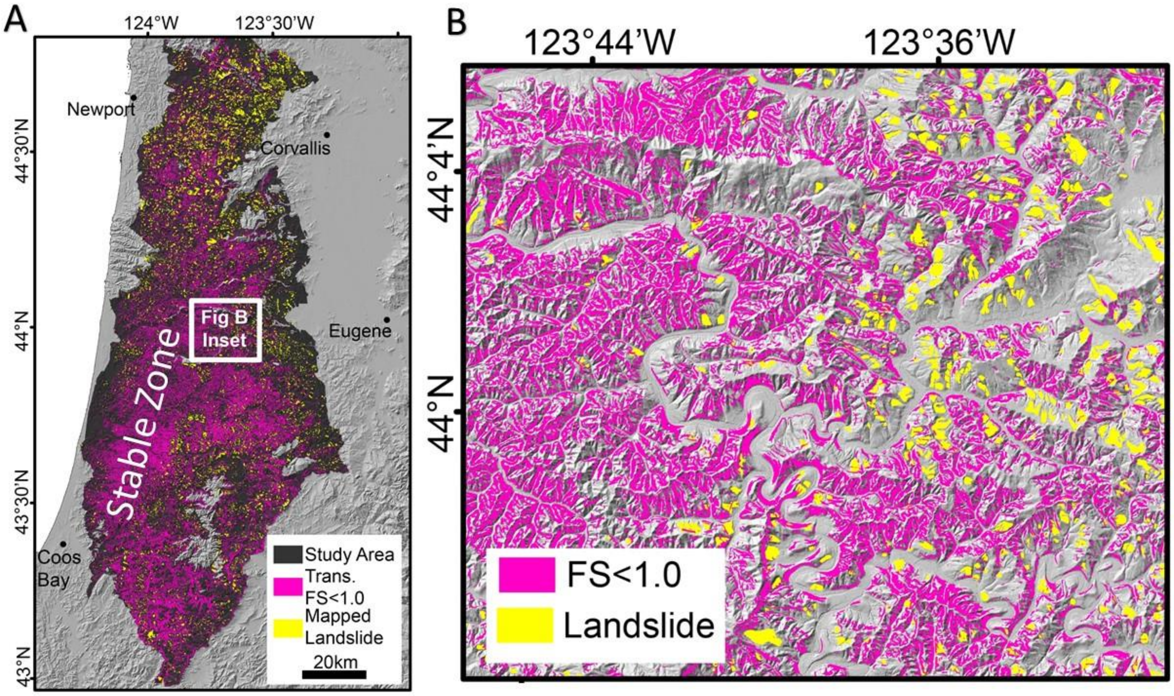

Figure A2. **A.** Modeled translational landslide susceptibility under saturated, static conditions and mapped landslide deposits across the study area (shaded region). 10m pixels with modeled factor of safety less than 1.0 shown in pink, landslides mapped manually from 1m lidar shown in yellow. **B.** Detailed inset map shows poor landslide susceptibility model performance. The model consistently overpredicts susceptibility in areas without mapped landslides and underpredicts in areas with high densities of mapped landslides.

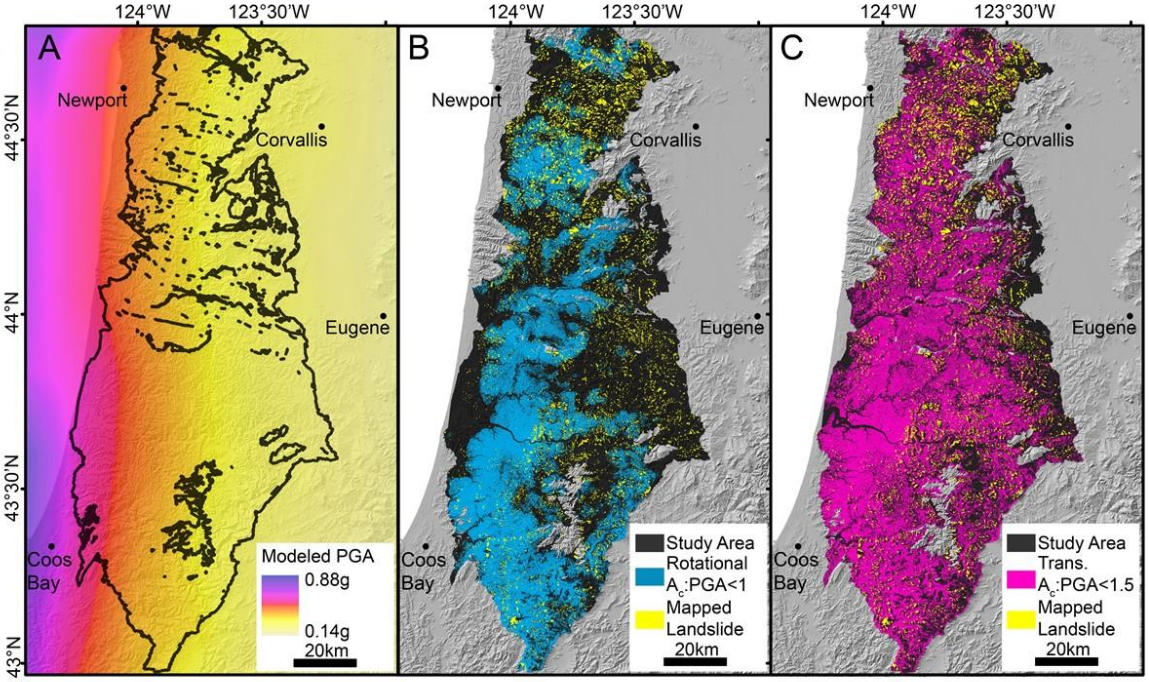

Figure A3. **A.** Modeled peak ground acceleration associated with average magnitude 9 Cascadia Subduction Zone megathrust earthquakes from Wirth et al. (2018) and Frankel et al. (2018). Original 20 km x 20 km smoothed to 10 m x 10 m across study area using bilinear interpolation. **B.** Modeled dynamic rotational landslide susceptibility during magnitude 9 earthquake under saturated conditions and mapped landslide deposits across the study area. Pixels with yield acceleration to peak ground acceleration ratios less than 1 shown in blue. Mapped landslides shown in yellow. **C.** Modeled dynamic translational landslide susceptibility during magnitude 9 earthquake under saturated conditions and mapped landslide deposits across the study area. Pixels with yield acceleration to peak ground acceleration ratios less than 1.5 shown in pink. Mapped landslides shown in yellow.

Appendix A Bibliography

Bandyopadhyay, A., & Abdullah, H. (2013). A Laboratory Study of Strong and Weak Sandstones.

Corominas, J., van Westen, C., Frattini, P., Cascini, L., Malet, J.P., Fotopoulou, S., Catani, F., Van Den Eeckhaut, M., Mavrouli, O., Agliardi, F. and Pitilakis, K., 2014. Recommendations for the quantitative analysis of landslide risk. Bulletin of engineering geology and the environment, 73(2), pp.209-263.

Frankel, A., Wirth, E., Marafi, N., Vidale, J., & Stephenson, W. (2018). Broadband synthetic seismograms for magnitude 9 earthquakes on the cascadia megathrust based on 3D simulations and stochastic synthetics, Part 1: Methodology and overall results. *Bulletin of the Seismological Society of America*, *108*(5A), 2347-2369.

Grant, A., Wartman, J., & Abou-Jaoude, G. (2016). Multimodal method for coseismic landslide hazard assessment. Engineering geology, 212, 146-160.

Guzzetti, F., Reichenbach, P., Ardizzone, F., Cardinali, M., & Galli, M. (2006). Estimating the quality of landslide susceptibility models. Geomorphology, 81(1-2), 166-184.

Jafarpour, M., Rahmati, H., Azadbakht, S., Nouri, A., Chan, D., & Vaziri, H. (2012). Determination of mobilized strength properties of degrading sandstone. Soils and Foundations, 52(4), 658-667.

Lu, N., & Godt, J. W. (2013). Hillslope hydrology and stability. Cambridge University Press.

Newmark, N., 1965. Effects of earthquakes on dams and embankments. Geotechnique 15, 139–160.

Pollock, W., Grant, A., Wartman, J., & Abou-Jaoude, G. (2019). Multimodal method for landslide risk analysis. MethodsX, 6, 827-836.

Varnes, D. J. (1978). Slope movement types and processes. Special report, 176, 11-33.

Wirth, E. A., Frankel, A. D., Marafi, N., Vidale, J. E., & Stephenson, W. J. (2018). Broadband synthetic seismograms for magnitude 9 earthquakes on the Cascadia megathrust based on 3D simulations and stochastic synthetics, Part 2: Rupture parameters and variability. *Bulletin of the Seismological Society of America*, *108*(5A), 2370-2388.

VITA

Sean LaHusen grew up in Vancouver, Washington. He graduated from Ridgefield High School in the Spring of 2009 and began attending Western Washington University in the Fall of 2009. He studied geology and earned a B.S. with honors in 2013. Before beginning graduate studies in Earth and Space Sciences at the University of Washington in the Fall of 2014, he travelled to Alaska to work as a Physical Science Technician at Kenai Fjords National Park during the summer of 2014. After finishing his PhD at the University of Washington, Sean is excited to begin a Mendenhall postdoctoral research position with the United States Geological Survey in Mountain View, California.